

Accretion disks around binary black holes of unequal mass: GRMHD simulations near decoupling

Roman Gold¹, Vasileios Paschalidis¹, Zachariah B. Etienne^{1,2,3,4}, Stuart L. Shapiro^{1,5}

¹*Department of Physics, University of Illinois at Urbana-Champaign, Urbana, IL 61801*

²*Physics Department & Joint Space-Science Institute,
University of Maryland, College Park, MD 20742*

³*Gravitational Astrophysics Laboratory, NASA Goddard Space Flight Center, Greenbelt, MD 20771*

⁴*Department of Mathematics, West Virginia University, Morgantown, WV 26506*

⁵*Department of Astronomy & NCSA, University of Illinois at Urbana-Champaign, Urbana, IL 61801*

and

Harald P. Pfeiffer^{6,7}

⁶*Canadian Institute for Theoretical Astrophysics, University of Toronto, ON M5S 3H8, Canada*

⁷*Canadian Institute for Advanced Research, Toronto, ON M5G 1Z8, Canada*

We report on simulations in general relativity of magnetized disks onto black hole binaries. We vary the binary mass ratio from 1:1 to 1:10 and evolve the systems when they orbit near the binary-disk decoupling radius. We compare (surface) density profiles, accretion rates (relative to a single, non-spinning black hole), variability, effective α -stress levels and luminosities as functions of the mass ratio. We treat the disks in two limiting regimes: rapid radiative cooling and no radiative cooling. The magnetic field lines clearly reveal jets emerging from both black hole horizons and merging into one common jet at large distances. The magnetic fields give rise to much stronger shock heating than the pure hydrodynamic flows, completely alter the disk structure, and boost accretion rates and luminosities. Accretion streams near the horizons are among the densest structures; in fact, the 1:10 no-cooling evolution results in a refilling of the cavity. The typical effective temperature in the bulk of the disk is $\sim 10^5 (M/10^8 M_\odot)^{-1/4} (L/L_{\text{edd}})^{1/4} \text{K}$ yielding characteristic thermal frequencies $\sim 10^{15} (M/10^8 M_\odot)^{-1/4} (L/L_{\text{edd}})^{1/4} (1+z)^{-1} \text{Hz}$. These systems are thus promising targets for many extragalactic optical surveys, such as LSST, WFIRST, and PanSTARRS.

PACS numbers: 04.25.D-, 04.25.dg, 47.75.+f

I. INTRODUCTION AND MOTIVATION

Supermassive black hole (SMBH) binaries can form in magnetized plasma following galaxy mergers, via bar-mode instability in rapidly rotating supermassive stars, or by other dynamical processes [1]. After formation, a combination of dynamical friction and gas-driven migration is likely to catalyze the binary inspiral into the gravitational radiation-driven regime [1–7]. The exact details of these processes, including the “last-parsec problem”, remain active areas of research (see e.g. [8–10] and references therein). As a result, event rates and population synthesis studies at this stage are highly uncertain [11].

The exciting prospect of a simultaneous observation of both electromagnetic (EM) and gravitational waves (GWs) arising from accreting binary BHBs makes these systems prime targets in the era of multi-messenger astronomy. Such observations will enable us to determine the binary masses, BH spins, redshift and even determine the Hubble constant to better than 1% [12–14].

Gravitational waves (GWs) from SMBHs are expected to be detected by planned GW interferometers such as eLISA/NGO detectors [15], sensitive to GW frequencies $10^{-5} - 1 \text{Hz}$, and the currently operating Pulsar Timing Arrays [16–18], sensitive to frequencies $10^{-9} - 10^{-6} \text{Hz}$. As SMBHs are typically believed to have masses in the range $10^6 - 10^9 M_\odot$, the GW strain at orbital separation $d = 10M$ - the value adopted in this work - is

$h \sim 10^{-16} (d/10M)^{-1} (M/10^8 M_\odot) (D/16 \text{Gpc})^{-1}$. Here M is the total mass of the binary, and we normalized to a luminosity distance D corresponding to redshift $z \simeq 2$ in a standard ΛCDM Universe. The corresponding gravitational-wave frequency is $f_{\text{GW}} \sim 10^{-4} (M/10^8 M_\odot)^{-1} (d/10M)^{-3/2} [(1+z)/3]^{-1} \text{Hz}$. The expected GW strain is above the eLISA strain sensitivity at these frequencies [15], hence these systems will be detectable by eLISA. In particular, for $M \sim 10^6 M_\odot$, the value of f_{GW} at $d = 10M$ falls well within the eLISA sensitivity band even for larger redshifts, while for $M \sim 10^8 M_\odot$ and large redshifts ($z \sim 10$), the value of f_{GW} at $d = 10M$ is marginally within the eLISA sensitivity band. However, the inspiral time from these separations is $t_{\text{GW}} \sim 20 (M/10^8 M_\odot)$ days assuming equal masses. Hence, these systems will quickly enter the eLISA sweet spot, and EM precursor signals can trigger targeted GW searches with a convenient lead time of several days.

While awaiting the first detection of GWs, currently operating and future electromagnetic (EM) detectors such as LSST [19], WFIRST [20] and PanSTARRS [21] are promising instruments to identify accreting BHB systems in the EM spectrum. Important steps have already been made toward realizing this goal.

Currently, we know of one spatially resolved SMBH binary candidate at an orbital separation $d \sim 7 \text{pc}$: 0402+379 [22]. Other spatially unresolved, SMBH bi-

nary candidates have been found, including OJ287 [23–26] and SDSS J1536+0441 [27, 28]. Binary AGN candidates have been singled out based on offsets in the broad line and narrow line regions, emission line profiles, and time variability [29, 30]. Recently, very-long baseline interferometric observations interpreted ejection components from AGN cores as undulations caused by the precession of the accretion disks around a SMBH binary [31]. A simplified model was applied to two AGN sources; for 1823+568 their analysis yields $d \sim 0.42\text{pc}$, and a mass ratio q in the range $0.095 < q < 0.25$, while for 3C 279 $d \sim 2.7\text{pc}$, $q \sim 0.36$. However, given the lack of a robust circumbinary accretion disk theory these results are at best preliminary. Nevertheless, they still motivate a study of accretion flows onto supermassive BH binaries with different mass ratios, which we initiate in this work in general relativity (GR).

Other features identified as “smoking guns” for binary black holes include BH recoil/kicks [32], used to explain the large velocity offsets between emission lines in AGN spectra, as well as observed kinks in jets probably due to changes in BH spin (X-shaped radio sources), a past merger event, or precession effects [33–35]. Modifications to the line profiles have also been proposed as promising characteristic features to distinguish binary BH AGN from classical, single BH AGN sources [36].

To assist and solidify all these detection efforts, it is crucial to identify and model possible electromagnetic “precursor” and “afterglow” signatures [37–43].

Depending on the physical regime the properties characterizing the gas can differ considerably, and different accretion models are applicable. For example, if the gas has little angular momentum, the accretion flow resembles the binary analog of a Bondi-Hoyle-Lyttleton solution [44–46] (see [47–49] for GR studies). If the gas has significant angular momentum, then the gas can become rotationally supported and form a disk.

For a BHBH embedded in a disk, one can identify several different regimes based on the time scales for migration of the binary. For a SMBH binary engulfed by a (thin) disk at large separation, the migration of the binary is initially governed by binary-disk angular momentum exchange mediated by (effective) viscosity [3]. At large enough separations, the reduced mass μ of the binary is less than the local interior disk mass ($4\pi d^2 \Sigma$ where Σ is the surface density of the disk). This leads to the so-called disk-dominated type II migration occurring on the viscous time scale t_{vis} . As the migration proceeds, the reduced mass of the system becomes larger than the local disk mass and the migration enters the secondary-dominated type II regime, which occurs on a longer time scale $t_{\text{sd}} \equiv (4\pi d^2 \Sigma / \mu)^{-k} \times t_{\text{vis}} \geq t_{\text{vis}}$, where k a constant of order ~ 0.4 if $4\pi d^2 \Sigma / \mu < 1$ and 0 otherwise. Ultimately, the binary enters a regime at smaller orbital separations where angular momentum losses due to GWs dominate, and the binary migrates on the GW time scale t_{GW} . In all regimes, the disk moves inwards on the viscous time scale. When $t_{\text{vis}} \leq t_{\text{sd}} < t_{\text{GW}}$ or

$t_{\text{vis}} < t_{\text{GW}} < t_{\text{sd}}$ the disk can follow the inspiral of the binary and settle in a quasi-steady state - this is called the *predecoupling* regime. When $t_{\text{GW}} < t_{\text{vis}}$, the binary decouples from the disk, i.e. the inward migration of the binary out-paces the inward drift of the disk.

In this paper we focus on the phase near *decoupling*, while the postdecoupling regime will be the subject of a future paper. We note that unlike eLISA, Pulsar Timing Arrays are sensitive only to SMBH binaries well within the predecoupling regime.

Accretion onto a single BH has been studied in great detail for decades, and magnetohydrodynamic studies in GR have drastically improved our understanding of these flows (see [50] for a recent review). Many different disk models have been proposed in the literature. These models range from geometrically-thin, optically thick disks [51, 52] and slim disks [53], to geometrically thick, optically thin, radiatively inefficient accretion flows (RIAF) [54–58]. However, our understanding of accretion flows onto BHBHs remains poor and studies of these systems are still in their infancy.

The first analytic Newtonian model and smooth particle hydrodynamic simulation of a circumbinary accretion disk was given in [59]. Since then, other Newtonian (semi-)analytic studies [40–42, 60, 61] and hydrodynamic simulations in 2D [62–65], and 3D [66–70] have followed. Newtonian magnetohydrodynamic (MHD) simulations were presented in [71], and Post-Newtonian MHD simulations in [72]. Many of these earlier studies excluded the binary and most of the inner cavity from the computational domain, introducing an artificial inner boundary condition. The importance of treating the inner regions self-consistently has been discussed in [69], and only full GR calculations can achieve this goal reliably.

A “GR-hybrid” orbit-averaged model for thin disks, in which the viscous part is handled in GR and the tidal torques in Newtonian gravity was introduced in [43], and GR hydrodynamical simulations of accretion onto BHBH binaries - taking into account the dynamical spacetime - have been performed in [47, 73–75]. To date the only GR magnetohydrodynamic (GRMHD) simulations of disk accretion onto BHBHs that account both for the dynamical spacetime and the BH horizons were presented in [76].

Using a different approach by assuming that the B-field is anchored to a circumbinary disk *outside* the computational domain, [77–80] modeled EM signatures by solving the GR force-free electrodynamic equations.

Close to merger a single BH remnant is formed on a time scale much shorter than the dynamical time scale in the disk. The mass and angular momentum of the remnant BH is different from the total mass and angular momentum prior to merger due to GW emission, causing a quasi-instantaneous perturbation to the disk. This effect has been modeled using hydrodynamical and MHD simulations in Newtonian gravity and in GR [81–85].

A realistic and ideal 3D global model for a *circumbinary* disk around a SMBH binary near the decoupling

radius requires: a) a fully relativistic treatment of gravitation in a *dynamical* spacetime, b) GRMHD for the plasma flow, c) realistic cooling processes, and d) radiative transfer in curved spacetime. Simulations incorporating these effects must also have high resolution and long integration times (several viscous time scales). However, including all these ingredients in one simulation would make these computations prohibitive, because the wall-clock times required to integrate for even ~ 5 viscous time scales at the inner disk radius at high resolution are far too long with current supercomputer resources. Thus, some of these ingredients must be relaxed in order to obtain a qualitative understanding of these systems. For this reason, the models in this work feature a) and b). High resolution is only adopted for a few models. In addition, we model radiative cooling by a simple cooling function and consider the extreme opposite limits of “rapid” cooling and “no cooling” to bracket the possibilities.

In this paper we study the effects of the binary mass ratio on the disk near decoupling. We vary the BHBH binary mass ratio $q \equiv M_1/M_2 \leq 1$, considering 1:1, 1:2, 1:4, 1:8 and 1:10 mass ratios. The mass ratio regime $0.1 \lesssim q \lesssim 1$ is shown to be of high astrophysical relevance in [86, 87]. Also, it has been argued that BHBHs forming in major galaxy mergers will typically have mass ratios in the range $(0.01, 1)$ [88]. These results motivate our choice of mass ratios. Note that Newtonian simulations studying the effects of mass ratio in the context of 2D thin-disk models were performed in [64, 65].

The new aspects of our work are the inclusion of relativistic gravitation to resolve the crucial physics near the BH horizons, effective viscosity arising from the magnetorotational instability [89, 90], geometrically thick disks, three spatial dimensions (3D), a Γ -law equation of state (EOS), and effective cooling. We model the decoupling epoch by fixing the binary separation d , evolving the spacetime by rotating our conformal-thin-sandwich initial data [91–94] as we have done in [76, 95]. The dependence of the flow variability, EM signatures, the magnetic field structure and the matter dynamics inside the low-density “hollow” on the mass ratio q are investigated. We estimate thermodynamic properties of the gas and scale our results with the binary total mass and the luminosity in units of the Eddington luminosity where feasible. From this, emission characteristics including typical thermal frequencies and luminosities are given and relevant detectors are discussed.

In the absence of any observational constraints on the thermodynamic state of accreting BHBHs, the models we consider in this work adopt an adiabatic EOS governed by an adiabatic index $\Gamma = 4/3$, appropriate for radiation pressure-dominated, optically thick disks. This choice is motivated in part both by theory and observations. First, accretion disk theory [50] predicts that the inner part of circumbinary disks around SMBH binaries are optically thick, radiation pressure dominated for a large set of possible disk parameters (see e.g. [4, 52] and the next

section). Furthermore, as discussed in [3], steady-state disk models predict that radiation pressure-dominated circumbinary disks will channel more material into the cavity for a given central mass. This finding makes radiation pressure-dominated circumbinary disks promising sources for electromagnetic counterparts.

Second, AGN data from the Sloan Digital Sky Survey (SDSS) [96–98], the AGN and Galaxy Evolution Survey (AGES) [99], XMM-COSMOS [100] and others [101] covering mostly type I AGNs and the local Universe to redshift of $z \lesssim 5$, reveal Eddington ratio distributions in the range $0.01 \lesssim L/L_{\text{Edd}} \lesssim 1$ with the tendency that higher L/L_{Edd} values occur at higher z (and possibly smaller central mass M). A comparison of accretion time scales with the age of the Universe suggests that earlier accretion episodes are closer to the Eddington limit, similar to the recently discovered quasar at $z \sim 7.1$ with a central mass of $M \sim 2 \times 10^9 M_{\odot}$ [102] accreting at $L/L_{\text{Edd}} \sim 1.2 \pm 0.5$. These surveys therefore motivate studies of disks accreting near the Eddington luminosity, for which radiation pressure is important. Moreover, radiation pressure-dominated disks accreting near the Eddington limit are more likely to be detectable, even at large cosmological redshifts.

This paper is structured as follows: In Sec. II we present a qualitative discussion of the range of parameters and the associated physical regimes for which our simulations are appropriate. In Sec. III we describe our methods and techniques for evolving the spacetime, fluid, and magnetic fields, as well as our simple cooling prescription. We also present the different cases we consider and list our diagnostics for characterizing the accretion flow and EM signatures. In Sec. IV we show several tests we performed to motivate our numerical setup. In Sec. V we present the results from our simulations. We conclude in Sec. VI with a summary of the main results and a discussion of future work.

Here and throughout we adopt geometrized units, where $G = c = 1$, unless otherwise stated.

II. QUALITATIVE CONSIDERATIONS

In this section we use the Shakura-Sunyaev/Novikov-Thorne thin-disk model [51, 52] to make rough analytic estimates regarding the physical regime our disk models probe. While the Shakura-Sunyaev/Novikov-Thorne model strictly applies to a viscous flow onto a single BH neglecting the binary tidal torques, we expect that our qualitative analysis will apply roughly to our circumbinary disk models, which have $H/R = \mathcal{O}(0.1)$, where H is the disk scale height. This expectation should be best realized outside the binary orbit because the ratio of the tidal to viscous torques decays quickly far away from the binary orbit (see e.g. Fig. 6 in [43]).

A. Radiation pressure dominance

1. Shakura-Sunyaev/Novikov-Thorne model

The simulations reported here apply to *any* total (ADM) binary black hole mass M and, since we neglect the self-gravity of the gas, to *any* rest-mass density ρ_0 , provided it has the same initial disk profile adopted here. The quantities that are fixed, in addition to the initial disk profile, are the adiabatic index Γ appearing in the adopted ideal gas EOS, the ratio of the initial magnetic-to-total disk pressure, the initial magnetic field profile, the initial binary separation and the cooling law. In this section we use the steady-state thin-disk solution for a Shakura-Sunyaev/Novikov-Thorne disk about a single BH of mass M to estimate the physical values of some of the gas dynamical quantities as functions of M and luminosity L . We show below that for a range of astrophysically relevant choices of these parameters the disk is thermal radiation pressure-dominated, and this fact motivates our setting $\Gamma = 4/3$.

Neglecting the perturbative role of the secondary tidal torque, the steady-state accretion flow in a geometrically thin disk is uniquely specified by the Shakura-Sunyaev viscosity parameter α , the central mass M and the accretion rate \dot{M} . The quantity \dot{M} is specified in turn by the disk luminosity L and efficiency ε . The Shakura-Sunyaev/Novikov-Thorne model [51, 52] describes a disk that is radiation pressure-dominated inside a radius r_{inner} . In this region the radiation to gas pressure ratio is [50]

$$\frac{P_{\text{rad}}}{P_{\text{gas}}} \sim 5.4 \times 10^5 \left(\frac{r}{20M}\right)^{-21/8} \left(\frac{\alpha}{0.1}\right)^{1/4} \left(\frac{M}{10^8 M_\odot}\right)^{1/4} \left(\frac{L}{L_{\text{Edd}}}\right)^2 \left(\frac{\varepsilon}{0.1}\right)^2, \quad (1)$$

where $\varepsilon \equiv L/\dot{M}c^2$ is the radiative efficiency, $L_{\text{Edd}} \simeq 1.3 \times 10^{46} (M/10^8 M_\odot) \text{erg/s}$, and we chose the normalization for the α parameter based on typical values found in our simulations. For a thin-disk model the efficiency ranges from 0.057 for a non-spinning BH to 0.42 for a maximally spinning BH, so we scale to a value residing between these limits. The size of the inner region is determined by the condition $P_{\text{rad}}/P_{\text{gas}} = 1$, for which Eq. (1) yields

$$r_{\text{inner}}/M \sim 3000 \left(\frac{\alpha}{0.1}\right)^{2/21} \left(\frac{M}{10^8 M_\odot}\right)^{2/21} \left(\frac{L}{L_{\text{Edd}}}\right)^{16/21} \left(\frac{\varepsilon}{0.1}\right)^{-16/21}. \quad (2)$$

The geometrically thick disks we evolve in this work extend radially out to $r_{\text{out}} \sim 100M - 200M$. Hence, when scaling the accretion rate such that our models accrete near the Eddington limit, our models are fully immersed in this inner radiation pressure-dominated region.

In this region the typical rest mass densities are [50]

$$\rho_0 \sim 5.5 \cdot 10^{-12} \left(\frac{r}{20M}\right)^{3/2} \left(\frac{\alpha}{0.1}\right)^{-1} \left(\frac{M}{10^8 M_\odot}\right) \left(\frac{\dot{M}}{2.3 M_\odot/\text{yr}}\right)^{-2} \frac{\text{g}}{\text{cm}^3} \quad (3)$$

$$\sim 5.5 \cdot 10^{-12} \left(\frac{r}{20M}\right)^{3/2} \left(\frac{\alpha}{0.1}\right)^{-1} \left(\frac{M}{10^8 M_\odot}\right)^{-1} \left(\frac{L}{L_{\text{Edd}}}\right)^{-2} \left(\frac{\varepsilon}{0.1}\right)^2 \frac{\text{g}}{\text{cm}^3}. \quad (4)$$

As we will show later, these characteristic values for $P_{\text{rad}}/P_{\text{gas}}$ and ρ_0 are comparable to the values found in our simulations.

The Shakura-Sunyaev/Novikov-Thorne model predicts that the effective optical depth to absorption is $\tau^* \simeq 0.02$ adopting the same normalizations as in the equation above. This well-known inconsistency near the Eddington limit of the Novikov-Thorne model is removed with the generalization to the slim disk model [53]. This model differs from a thin disk in that it allows for cooling to occur via advection, which dominates radiative cooling at high accretion rates ($L \gtrsim 0.3L_{\text{Edd}}$), thereby puffing up the disk. When scaling our models to accrete near the Eddington limit, they are closer to slim-disk models, which remain optically thick in this high luminosity limit [50, 53].

As we discuss later, near the Eddington limit and $M = 10^8 M_\odot$, the effective optical depth satisfies $\tau^* \gtrsim 1$ in the bulk of our disk models, implying that the gas is optically thick to absorption and the photons eventually *thermalize*. Thus, these qualitative considerations motivate the adoption of an adiabatic index $\Gamma = 4/3$, appropriate for thermal radiation pressure dominance.

Note also that alternative disk models have been proposed, e.g. [4]. However, they largely share the prediction that the inner regions of the disk are radiation pressure dominated.

2. Decoupling radius

We estimate the decoupling radius a_d by equating $t_{\text{GW}} = t_{\text{vis}}$ and solve for the separation to find [76]

$$\frac{a_d}{M} \approx 13.3 \left(\frac{\alpha}{0.1}\right)^{-2/5} \left(\frac{H/R}{0.3}\right)^{-4/5} \left(\frac{\tilde{\eta}}{1}\right)^{2/5} \quad (5)$$

where we assumed that the inner disk edge radius settles to $r_{\text{in}} \approx 1.5d$ as typically found in our simulations, α is the Shakura-Sunyaev turbulent viscosity parameter, and $\tilde{\eta} \equiv 4q/(1+q)^2$ (see also [5]). Notice that in contrast to geometrically thick disks, where the decoupling radius is a few tens of M , geometrically thin disks have $a_d/M \simeq 100$. The decoupling radius estimate (5) for the mass ratios considered in this work ranges from $a_d(q=0.1) \approx 8.5M$ to $a_d(q=1) \approx 13.3M$. The normalizations in Eq. (5) are based on typical values obtained

from our simulations. We choose the binary separation $d \sim 10M$ for all cases studied in this work, a value which is consistent with the crude estimate of Eq. (5). In the future we intend to start our evolutions at larger separations in order to dynamically determine the decoupling radius and evolve through it as in [43].

III. METHODS

The models we adopt here assume: a) circular binary orbits, neglecting the binary inspiral (justified for large separations; see Sec. II A 2), b) non self-gravitating disks, which likely is a good assumption (see, e.g. [103]), c) ideal MHD, d) no radiative feedback, e) an effective cooling scheme that brackets no cooling and rapid cooling.

Some of these assumptions may not be obeyed strictly, e.g. the binary may become eccentric in the precoupling regime [6, 66–69, 104], or radiative feedback may become important near Eddington accretion rates. However, our simulations still provide a qualitative understanding of the physics that will be useful in designing the next set of more realistic models of binary black holes immersed in circumbinary disks. In this section, we describe the initial data and computational methods we adopt to account for a)-e).

A. Initial data and AMR hierarchy

1. Metric initial data

At large separation the binary inspiral time scale is much longer than the binary orbital period and the viscous time scale at the inner edge of the disk just beyond the binary orbit. Accordingly, the inspiral can be neglected over many orbital periods. To model this epoch in GR, we adopt quasi-equilibrium conformal-thin-sandwich (CTS) solutions for the black hole binary [91–94]. The spacetime initial data satisfying the CTS equations correspond to a circular orbit and possess a helical Killing vector. The CTS initial data have been generated using the spectral techniques described in [105] as implemented in the Spectral Einstein Code (SpEC) [106] (see also [107]). We list the initial data parameters describing our spacetimes in Table I.

2. Matter and B-field initial data

For the fluid we use the same family of equilibrium disk models around single BHs as in [95, 108, 109]. We choose the initial inner disk edge radius $r_{in,0} = 18M$ and specific angular momentum $l(r_{in,0}) = 5.15M^2$ around a non-spinning BH as in [76]. However, the disk model is

TABLE I. CTS initial data parameters for the BHBH vacuum spacetime. Columns show mass ratio (q), ADM mass (M_{ADM}) and angular momentum (J_{ADM}), and irreducible masses (M_{irr}^i), and apparent horizon radii (r_{hor}^i) for the two black holes. Diagnostics generating these quantities, but computed from vacuum, test simulations agree with these values to within one part in 10^4 .

q	M_{ADM}	J_{ADM}	M_{irr}^1	M_{irr}^2	r_{hor}^1	r_{hor}^2
1 : 1	0.98989	0.96865	0.50000	0.50000	0.42958	0.42958
1 : 2	0.99097	0.85933	0.66667	0.33333	0.60192	0.27312
1 : 4	0.99342	0.61603	0.80000	0.20000	0.75140	0.15832
1 : 8	0.99589	0.37868	0.88889	0.11111	0.85640	0.08618
1 : 10	0.99656	0.31652	0.90909	0.09091	0.88081	0.07022

not identical to [76] due to the different polytropic index ($\Gamma = 4/3$ here versus $\Gamma = 5/3$ in [76]).

We seed the initial disk with a small, purely poloidal B-field using the same procedure as in [76, 110]; see Fig. 1. The field is dynamically unimportant initially: the initial maximum value for the ratio of magnetic P_M to total pressure P is 0.025. All cases we consider in this work are initialized with the same disk and magnetic field.

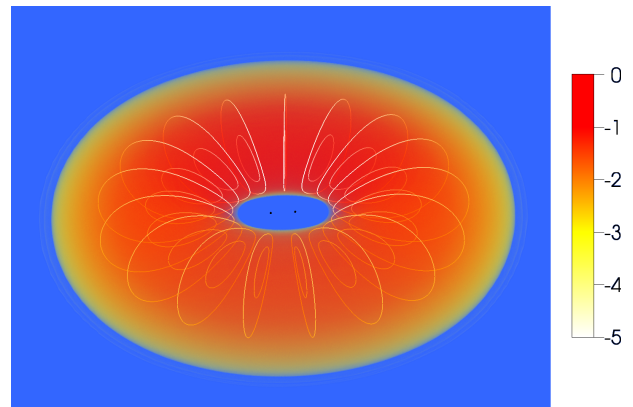


FIG. 1. B-field lines (white curves) and volume rendering of rest-mass density normalized to its maximum value at $t = 0$. The two black dots at the center indicate the BH apparent horizons for the $q = 1$ case.

Although we will qualitatively discuss how the evolution of these matter initial data depends on the binary mass ratio, it is important to stress that the goal of our work is to assess how the *final relaxed state* of the disk depends on the binary mass ratio. The initial data, which governs the early evolution, has no physical significance.

B. Evolution equations and techniques

1. GRMHD evolution

We use the Illinois GRMHD adaptive-mesh-refinement (AMR) code [111–113], which adopts the Cactus/Carpet

infrastructure [114–116]. This code has been extensively tested and used in the past to study numerous systems involving compact objects and/or magnetic fields (see e.g. [110, 117–121]), including black hole binaries in gaseous media [47, 76, 95].

The code solves the equations of ideal GRMHD in a flux-conservative formulation [see Eqs. (27)–(29) in [112]] employing a high-resolution-shock-capturing scheme (see [111, 112] for details), and including effective cooling source terms [see Eqs. (65) and (66) in [117]]. To enforce the zero-divergence constraint of the magnetic field, we solve the magnetic induction equation using a vector potential formulation [see Eq. (9) in [113]]. As our EM gauge choice we use the generalized Lorenz gauge condition we developed in [76] and used in [118, 121]. We choose the damping parameter $\xi = 8/M$. The advantage of this gauge condition is that it leads to *damped*, propagating EM gauge waves preventing spurious magnetic fields from arising near AMR boundaries even more effectively than the standard Lorenz gauge choice ($\xi = 0$) [113]. The damping properties of the generalized Lorenz gauge are crucial for stable and accurate long-term GRMHD evolutions. The “algebraic” gauge condition used in the first GRMHD simulations adopting A-field evolution (see e.g. [49, 112, 122]) was shown in [113] to suffer from spurious conversion of EM gauge modes into physical modes and vice-versa, due to interpolation at AMR boundaries. These spurious magnetic fields contaminate the evolution and the effect is exacerbated when matter crosses refinement boundaries.

To close the system of equations we use a Γ -law EOS

$$P = \rho_0 \epsilon (\Gamma - 1), \quad (6)$$

where P is the total pressure, ρ_0 the rest-mass density, and ϵ the specific internal energy. This EOS allows for shock heating. We choose $\Gamma = 4/3$ appropriate for radiation pressure-dominated, optically thick disks.

2. Metric evolution

The metric evolution is treated under the approximation that the inspiral time scale due to GW emission is long compared to both the binary orbital period and the viscous time scale of the disk. Hence, we can neglect the inspiral for multiple binary orbits. The CTS initial data we adopt possess a helical Killing vector, which implies that the gravitational fields are stationary in a frame corotating with the binary. As a result, we can perform the metric evolution in the center-of-mass frame of the binary by simply rotating the initial spacetime fields as was done in [47, 76]. This technique simplifies our computations substantially. In addition, the rotating metric method facilitates our evolving dynamically to relaxed disk/magnetic field initial data for the inspiral.

To implement this method, we map the CTS solution from the spectral grid onto three grids corresponding to three partially overlapping spherical coordinate systems:

One spherical coordinate system covers the entire evolution domain and is centered on the binary center of mass, and two smaller ones are centered on each BH. These new grids employ a logarithmic radial coordinate. We use the CTS solution stored on these spherical grids to interpolate the data onto the Cartesian evolution grids whenever we perform the rotation transformation.

We have checked that the mapping from the spectral grid to the spherical grids is implemented correctly by performing vacuum simulations that use the CTS solution stored in the spherical grids as initial data. More specifically, we have computed several diagnostic quantities which characterize the BHs and the global spacetime and compared them with the values known from the spectral CTS initial data (see Table I). These agree to within 1 part in 10^4 . Moreover, we have verified that a crude estimate for the orbital frequency of the binary (orbital trajectory traverses a full phase of 2π) as determined by a dynamical vacuum evolution agrees with the value given by the initial data ($M\Omega = 0.028$) to within $\sim 10\%$. We have computed the normalized $L_{2,N}$ norm of the Hamiltonian and momentum constraint violations as introduced in Eqs. (59) and (60) in [123], with the modification that we split up the Laplacian operator into its individual components when computing normalized norms. We find the normalized norm of the Hamiltonian constraint to be dominant, with $L_{2,N}(\mathcal{H}) \sim 2\%$. We conclude that the CTS solutions are mapped correctly and accurately.

3. Cooling

Without cooling, the binary tidal and the viscous torques act to gradually heat and puff up the disk. “Advective” cooling, which is crucial in slim-disk and ADAF models [50], is self-consistently accounted for in our simulations. However, adding radiative cooling may be necessary to achieve a steady state. Realistic radiative cooling based on actual physical mechanisms depends on complicated microphysics, which we do not model here, but intend to incorporate in future studies. To model steady-state solutions in this work, we introduce “radiative” cooling via an effective cooling leakage scheme. This scheme is, strictly speaking, valid in the optically thin regime. While this is a very crude approach to radiative cooling, treating both extremely rapid radiative cooling as well as no radiative cooling can help bracket the possibilities. Different formulae for the cooling emissivity Λ have been proposed in the literature:

I. Non-exponential cooling [72, 124]:

$$\Lambda = \frac{\rho_0 \epsilon}{\tau_{\text{cool}}} \left(\frac{\Delta S}{S_0} + \left| \frac{\Delta S}{S_0} \right| \right), \quad (7)$$

where $S \equiv K = \frac{P}{\rho_0}$ is an entropy parameter, and S_0 the initial target value. We call this emissivity “non-exponential”, because the effective cooling

time scale for this scheme is not just τ_{cool} , but depends on the internal energy ϵ (see Appendix A).

II. Exponential cooling [117, 119]

$$\Lambda = \frac{\rho_0 \epsilon_{th}}{\tau_{\text{cool}}} = \frac{\rho_0 \epsilon_0}{2\tau_{\text{cool}}} \left(\frac{\Delta S}{S_0} + \left| \frac{\Delta S}{S_0} \right| \right), \quad (8)$$

where ϵ_0 is the internal energy calculated using S_0 , and $\epsilon_{th} = \epsilon - \epsilon_0$. In this scheme the effective cooling time scale is τ_{cool} .

Both emissivities dissipate all shock-induced thermal energy, driving the entropy of the gas to its initial value. We use prescription II, instead of I, because we have found that prescription I is prone to the development of a Courant instability, as the *effective* cooling time scale of this scheme depends on the amount of shock heating, which can be very strong in low-density regions (see e.g. Appendix B in [125]). Thus, to stabilize the simulations with prescription I, one typically excludes cooling of the low-density regions or unbound matter [72, 76]. As both the BH horizons and the low-density cavity is included in our computational domain (unlike earlier studies), we find that the strong shock heating inside the cavity in conjunction with emissivity I leads to a numerical instability. In order to bracket the effect of cooling, this inner cavity needs to be cooled when cooling is enabled. In Appendix A, we present an analytic calculation illustrating the above considerations. We demonstrate that shock heating of matter in the cavity is important in Sec. IV C.

To model “rapid” radiative cooling we set the cooling time scale equal to 10% of the local, Keplerian time scale $\tau_{\text{cool}}/M = 0.1\tau_{\text{Kep}}/M = 0.1 \cdot 2\pi(r/M)^{3/2}$, where r is the cylindrical radial coordinate measured from the center of mass of the binary. In order to prevent the cooling time from becoming prohibitively small as $r \rightarrow 0$ we floor the cooling time at $\tau_{\text{cool}} \geq 10M$. Throughout this paper we refer to cases with $\Lambda \neq 0$ as the cooling cases and $\Lambda = 0$ as the no-cooling cases.

4. Evolution grids & models

We use a hierarchical, box-in-box adaptive mesh provided by the Cactus/Carpet infrastructure [115, 116]. We constructed two sets of nested boxes, with one set centered on each BH, on which we discretize the GRMHD evolution equations. The coarsest level has an outer boundary at $r = 240M$. Due to a range of resolution requirements related to the different sizes of the BHs, different models use different number of refinement levels, which in turn yields different finest grid spacings (see Table II). We set up the locations of our AMR boundaries such that the computational grids resolve both the BHs and the inner disk region for the given resources.

The grid spacing is also motivated by both MRI resolution requirements and the results gleaned from test runs involving hydrodynamic disk evolutions around a single, non-spinning BH, which we report on in Sec. IV.

In Table II we also list the distinguishing characteristics of the different cases we consider in this work. The labels are chosen to designate the mass ratio, whether cooling is applied or not, and the resolution. For example, the label 1:1nc-hr means mass ratio $q = 1$, no-cooling, and high resolution.

We point out that the disparity in length scales (horizon vs. disk size) and time scales (the Courant condition vs. viscous time scale) intrinsic to the circumbinary BHs disk problem introduces a large computational cost. Most of our simulations were run continuously (excluding queue waiting times) for ~ 2 months on **Blue Waters**, **Kraken**, **Lonestar**, as well as the Illinois Relativity group 36-node Beowulf cluster. The CPU hours used depended on the computer cluster, but we estimate that the simulations presented here required $\sim 2 \times 10^6$ CPU hours.

C. Diagnostics

We distinguish two types of diagnostics. The first type consists of probes of the MHD flow, including the density and velocity profiles, accretion rates, luminosity estimates, magnetic field profiles, the establishment of MRI turbulence and jets, etc. The second type concerns properties of the plasma such as local temperatures, optical depths, characteristic frequencies of emitted radiation, etc. The first type are straightforward to calculate from our simulation data, as they depend on the overall MHD behavior of the disk, and once we have chosen an EOS and cooling prescription, are independent of detailed microphysics. We are quite careful and confident in reporting these diagnostic quantities. The second type depends crucially on the specific physical values we assign to our nondimensional input parameters (e.g. BH mass and disk density) and to the microphysics that is not incorporated in our calculation (e.g. realistic radiative cooling and radiative transport). Nevertheless, we can make crude estimates for the latter quantities, and do so below. Although considerable caution must be applied to these estimates, they may serve as useful guides to subsequent, more detailed investigations and to astronomical instruments that may be able to observe the scenarios we are simulating.

The first type of diagnostics includes: 1) Accretion rate \dot{M} as defined in [47]. We compute the total accretion rate onto the binary, and also the accretion rate onto each individual BH. 2) Fourier analysis of the accretion rate $FFT(\dot{M})$, targeted to identify possible quasiperiodic signatures in the accretion flow. 3) Surface density profile $\Sigma(r)$ as defined in [95]. This diagnostic is also useful to compare with studies of 1D orbit-averaged disk models. 4) Shakura-Sunyaev α -stress parameter

TABLE II. List of grid parameters for all models. Equatorial symmetry is imposed in all cases. The computational mesh consists of two sets of nested AMR grids, one centered on each BH, with the outer boundary at $240M$ in all cases. From left to right the columns indicate the case label, mass ratio q , whether cooling is included or not, the coarsest grid spacing Δx_{\max} , number of AMR levels around the primary (BH) and the secondary (bh), and the half length of each AMR box centered on each BH. The grid spacing of all other levels is $\Delta x_{\max}/2^{n-1}$, $n = 1, 2, \dots, n_{\max}$, where n is the level number such that $n = 1$ corresponds to the coarsest level. A dash “—” indicates “no information available”.

Case	q	cooling?	Δx_{\max}	levels(BH)	levels(bh)	Grid hierarchy
1:1nc-hr	1:1	No	$4.8M$	7	7	$240M/2^{n-1}$, $n = 2, \dots, 5$, $240M/2^n$, $n = 6, 7$
1:1nc-mr	1:1	No	$6.0M$	7	7	$240M/2^{n-1}$, $n = 2, \dots, 5$, $240M/2^n$, $n = 6, 7$
1:1nc-lr	1:1	No	$8.0M$	7	7	$240M/2^{n-1}$, $n = 2, \dots, 5$, $240M/2^n$, $n = 6, 7$
1:2nc-lr	1:2	No	$8.0M$	7	8	$240M/2^{n-1}$, $n = 2, \dots, 5$, $240M/2^n$, $n = 6, 7, 8$
1:4nc-lr	1:4	No	$8.0M$	7	9	$240M/2^{n-1}$, $n = 2, \dots, 5$, $240M/2^n$, $n = 6, \dots, 9$
1:8nc-lr	1:8	No	$8.0M$	6	10	$240M/2^{n-1}$, $n = 2, \dots, 5$, $240M/2^n$, $n = 6, \dots, 10$
1:10nc-lr	1:10	No	$8.0M$	6	10	$240M/2^{n-1}$, $n = 2, \dots, 5$, $240M/2^n$, $n = 6, \dots, 10$
0nc-hr	0	No	$4.8M$	6	—	$240M/2^{n-1}$, $n = 2, \dots, 5$, $240M/2^n$, $n = 6$
0nc-mr	0	No	$6.0M$	6	—	$240M/2^{n-1}$, $n = 2, \dots, 5$, $240M/2^n$, $n = 6$
0nc-lr	0	No	$8.0M$	6	—	$240M/2^{n-1}$, $n = 2, \dots, 5$, $240M/2^n$, $n = 6$
1:1c-mr	1:1	Yes	$6.0M$	7	7	$240M/2^{n-1}$, $n = 2, \dots, 5$, $240M/2^n$, $n = 6, 7$
1:2c-lr	1:2	Yes	$8.0M$	7	8	$240M/2^{n-1}$, $n = 2, \dots, 5$, $240M/2^n$, $n = 6, 7, 8$
1:4c-lr	1:4	Yes	$8.0M$	7	9	$240M/2^{n-1}$, $n = 2, \dots, 5$, $240M/2^n$, $n = 6, \dots, 9$
1:8c-lr	1:8	Yes	$8.0M$	6	10	$240M/2^{n-1}$, $n = 2, \dots, 5$, $240M/2^n$, $n = 6, \dots, 10$
1:10c-lr	1:10	Yes	$8.0M$	6	10	$240M/2^{n-1}$, $n = 2, \dots, 5$, $240M/2^n$, $n = 6, \dots, 10$
0c-lr	0	No	$8.0M$	6	—	$240M/2^{n-1}$, $n = 2, \dots, 5$, $240M/2^n$, $n = 6$

computed as $\alpha \sim \alpha_{\text{EM}} \equiv \langle \frac{\langle T_{\hat{r}\hat{\phi}}^{\text{EM}} \rangle}{\langle P \rangle} \rangle_t$ where $T_{\hat{r}\hat{\phi}}^{\text{EM}}$ is the dominant orthonormal component to the Maxwell stress-energy tensor evaluated using the tetrad defined in [126] (the brackets denote an orbit averaged quantity). More specifically, we report an azimuthally- and z -averaged $\alpha = \alpha(r)$ profile, which can be used in 1D orbit-averaged disk models. 5) Disk scale height $H = \Sigma/\rho_0(z = 0)$. 6) Inner disk edge radius r_{in} : In all $\Sigma(r)$ -profiles we observe that inside the cavity $\Sigma(r)$ declines rapidly with decreasing r and becomes convex. We fit a fifth order polynomial to the orbit-averaged $\Sigma(r)$ in the convex region at small r , and define r_{in} as the radius where the curvature of the $\Sigma(r)$ fitting function is maximized, $[\Sigma''(r)/(1 + \Sigma'(r)^2)^{3/2}]' = 0$ where $' \equiv d/dr$. 7) EM Poynting luminosity (L_{EM}) as defined in Eq. (1) of [121]. 8) Energy loss rate carried off by the outflowing gas $L_{\text{gas}} = \oint_s T_{0,(\text{gas})}^r dS$. This surface integral must be performed in the asymptotically flat regime. Given that we do not perform the integration at an infinite radius, as a crude approximation to L_{gas} we include in the integration only matter that is unbound, i.e., matter for which at large radii $E = -u_0 > 1$. We compute 7) and 8) at several radii including $90M, 140M, 210M$. 9) For cases where our cooling scheme is enabled, we compute the cooling luminosity $L_{\text{cool}} = \oint_s T_{0,(\text{rad})}^r dS$, which we estimate via the volume integral $L_{\text{cool}} = \int \Lambda u_0 \alpha \sqrt{\gamma} d^3x$. The volume integration is exactly equal to the surface integration at steady-state and in spacetimes possessing a timelike Killing vector and when we ignore any radiation captured by the BHs. We also compute the bolometric

radiative luminosity $L_b = L_{\text{EM}} + L_{\text{cool}}$.

The second type of diagnostics includes: 10) Optical depth to true absorption $\tau^* = \sqrt{3}\tau_{\text{es}}\tau_{\text{ff}}$ (Eddington approximation), where we assume pure hydrogen and where τ_{es} (τ_{ff}) is the optical depth to electron scattering (free-free absorption), calculated using the Thompson scattering opacity $\kappa_{\text{es}} = 0.4\text{cm}^2/\text{g}$ (Rosseland mean opacity $\bar{\kappa}_{\text{ff}} = 6.45 \cdot 10^{23} \rho_0 T^{-3.5} \text{cm}^2/\text{g}$) as $\tau_{\text{es}} = \kappa_{\text{es}}\Sigma$ ($\tau_{\text{ff}} = \bar{\kappa}_{\text{ff}}\Sigma$) [127]. $\tau^* > 1$ implies the matter is optically thick to absorption. 11) Local temperature of the matter, calculated by solving $\epsilon = aT^4/\rho_0 + 2k_B T \rho_0/m_p$, where m_p is the proton mass and k_B the Boltzmann constant. 12) In the cases with cooling, the effective disk temperature (in cooling cases), estimated by assuming that all cooling luminosity is emitted as black body radiation:

$$T_{\text{eff}} = [L_{\text{cool}}/4\pi\sigma(r_{\text{out}}^2 - r_{\text{in}}^2)]^{1/4}, \quad (9)$$

where σ is the Stefan-Boltzmann constant and r_{out} is the disk outer radius. 13) Characteristic observed thermal radiation frequencies $\nu_{\text{bb}} = k_B T_{\text{eff}}/h(1+z)$, where h is the Planck constant and z the cosmological redshift. This is calculated only when $\Lambda \neq 0$. 14) Cyclotron emission. While we find the bulk of the disk to be optically thick near Eddington accretion rates, the low-density “cavity” is optically thin. From these regions cyclotron lines may be detectable. 15) In cases where $\Lambda \neq 0$ we compute the characteristic cyclotron frequencies $\nu_{\text{cy}} = eB/mc(1+z)$, where e is the electron charge, m the electron mass and B the magnitude of the magnetic field.

IV. TESTS AND RESOLUTION REQUIREMENTS

In this section we describe tests we performed that motivate the choices for the grid resolution and cooling time scale.

A. Hydrodynamical evolutions with $B = 0$

To set a lower limit on the necessary resolution to perform our GRMHD simulations, we found the minimum resolution required so that our code maintains stable equilibrium of an unmagnetized disk around a single non-spinning BH for several thousands of M of evolution. The equilibrium disk solution we use is described at the beginning of Sec. III A 2. Our study indicates that for the low resolution ($\Delta x_{\max} = 8.0M$) listed in Table II the surface density profile of the initial disk is maintained to within 2% throughout the disk for at least $t \sim 5000M$.

B. MRI resolution requirements

Here we check the conditions for MRI to operate in our disk models. For this to be the case three conditions have to be satisfied: (I) A magnetic field configuration must be present that violates the stability condition for MRI $d\Omega/dr \geq 0$, (II) The wavelength of the fastest-growing mode λ_{MRI} has to be resolved by $\gtrsim 10$ gridpoints [128–130], and (III) the B-field must be sufficiently weak for $\lambda_{\text{MRI}} \lesssim 2H$. In other words the wavelength of the fastest growing mode should fit in the disk [131].

Regarding (I) our initial disk model is unstable to the MRI because of the outwardly decreasing angular velocity and the presence of an initially small poloidal magnetic field. Regarding (II) we plot the quality factor $Q \equiv \lambda_{\text{MRI}}/dx$ where dx is the local grid spacing (which jumps by a factor of two at AMR boundaries); see Fig. 2. One can see that we satisfy the criterion $Q \gtrsim 10$ over a rather large portion of the disk initially except for the region near the radius where the poloidal field changes sign and becomes very small. We chose our low-resolution grids such that condition (II) is satisfied at $t = 0$ in the innermost parts of the disk.

Regarding (III) we plot a meridional (x, z) - slice of the rest-mass density overlaid by a line plot showing λ_{MRI} as a function of x in Fig. 3. The plot shows that for the most part λ_{MRI} fits within the disk. At the inner disk edge the MRI is likely to be suppressed initially, but as the evolution proceeds magnetic winding converts poloidal fields into toroidal ones lowering λ_{MRI} and eventually triggering the MRI near the inner disk-edge.

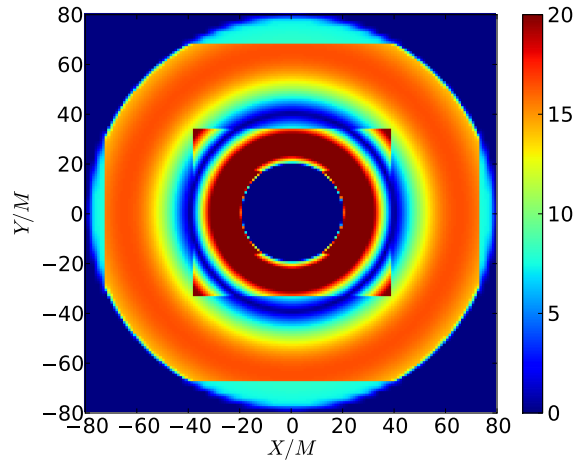


FIG. 2. Contours of the λ_{MRI} -quality factor $Q = \lambda_{\text{MRI}}/dx$ in the equatorial plane, corresponding to the equal mass ($q = 1$) medium resolution case [divide (multiply) by 1.33 (1.25) for the low (high) resolution case] at $t = 0M$. We resolve the fastest growing MRI mode by $\gtrsim 10$ gridpoints over a large part of the disk (the blue ring stems from extremely small values of λ_{MRI} , when the vertical component of the B-field changes sign).

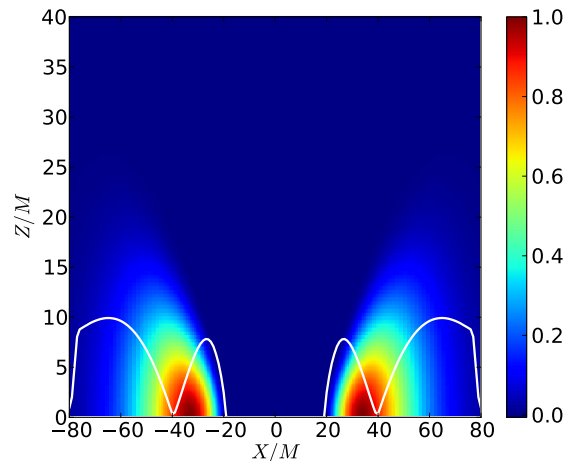


FIG. 3. Rest-mass density contours (color coded) on a meridional slice, and $\lambda_{\text{MRI}}/2$ (black solid line) at $t = 0M$. The plot corresponds to equal mass ($q = 1$) but is the same among all cases considered in this work. For the most part $\lambda_{\text{MRI}}/2$ fits within disk.

C. Cooling

We seek to compare two opposite limiting cases for each mass ratio: (I) No-cooling, $\tau_{\text{cool}} \gg \tau_{\text{Kep}}$ for which $\Lambda = 0$. Here τ_{Kep} is the local Keplerian time scale which is comparable to the (shock) heating time scale; (II) extremely rapid cooling, $\tau_{\text{cool}} \ll \tau_{\text{Kep}}$ which we model with the effective emissivity $\Lambda = \frac{\rho_0 \epsilon_{\text{th}}}{\tau_{\text{cool}}}$.

To determine the value for τ_{cool} at which cooling becomes rapid (at least in the bulk of the disk), we performed the $q = 1$ cooling case using different cooling time scales. We concluded that rapid cooling requires a cooling time scale significantly shorter than the local Keplerian time scale. In Fig. 4, we plot K/K_0 , where the entropy parameter $S \equiv K = P/(\rho_0^\Gamma)$ and $S_0 = K_0 = K(t = 0)$ for a run with $\tau_{\text{cool}} = 0.1\tau_{\text{Kep}}$ (left panel), a run with $\tau_{\text{cool}} = \tau_{\text{Kep}}$ (middle panel) and a run without cooling $\tau_{\text{cool}} = \infty$ (right panel). It becomes apparent that when $\tau_{\text{cool}} = \tau_{\text{Kep}}$, K is not driven back to its initial value. Physically, this means that not all shock generated entropy is radiated away, hence $\tau_{\text{cool}} = \tau_{\text{Kep}}$ does not correspond to rapid cooling and steady state is not achieved. For $\tau_{\text{cool}} = 0.1\tau_{\text{Kep}}$ we find $K/K_0 \sim 1$ in the bulk of the disk. The values depart from unity only inside the cavity where low density gas exists and can be shock heated to very high K/K_0 , demonstrating that shock heating is extremely strong in the low-density cavity. We adopt $\tau_{\text{cool}} = 0.1\tau_{\text{Kep}}$ in all our cooling simulations because it leads to rapid cooling, at least throughout the bulk of the disk.

V. RESULTS

In this section we present the results of our numerical simulations. First, in Sec. VA we show results from our resolution study. In Sec. VB, we directly compare the $q = 1$ binary case with $B \neq 0$ to the $B = 0$ case. Lastly, we report on the variation of our diagnostics with mass ratio for all magnetized cases in Sec. VC.

Our simulations have two parameters that scale out of the problem: the total mass of the BHBH binary M and the rest-mass density of the disk. Alternatively, we can exchange one of these parameters with another parameter that depends on these two free parameters. So, instead of the rest-mass density, in the results we quote we choose the Eddington ratio L_b/L_{Edd} , where L_b is the bolometric EM luminosity described in Sec. III C. The relation between these parameters is determined as follows: the accretion rate through the horizon must scale like $\dot{M} \propto \rho_{0,\text{ref}} M^2$, where $\rho_{0,\text{ref}}$ is a reference rest-mass density in the disk. We choose the maximum rest-mass density at $t = 0$ as the reference density, and our simulations determine the proportionality constant. For example, in the single, nonspinning BH case with cooling we find

$$\rho_{\text{ref}} = 9 \times 10^{-12} \left(\frac{L_b}{L_{\text{Edd}}} \right) \left(\frac{M}{10^8 M_\odot} \right)^{-1} \text{ g cm}^{-3},$$

where we have replaced the accretion rate via the following expression

$$\begin{aligned} \dot{M} &= L_b \varepsilon^{-1} = \left(\frac{L_b}{L_{\text{Edd}}} \right) L_{\text{Edd}} \varepsilon^{-1} \\ &\approx 2.75 \left(\frac{L_b}{L_{\text{Edd}}} \right) \left(\frac{M}{10^8 M_\odot} \right) M_\odot \text{ yr}^{-1}, \end{aligned} \quad (10)$$

and where $\varepsilon \equiv L_b/\dot{M} = 0.08$ is the radiative efficiency as computed via our simulations for our adopted cooling law in the single, nonspinning BH case. In the no-cooling cases the only radiation luminosity estimate we have is the Poynting luminosity which is expected to be a small fraction of the total radiative luminosity. Hence, in the no-cooling cases we do not scale our results with the Eddington ratio. Instead, we choose a fiducial accretion rate similar to the one given in Eq. (10).

A. Resolution study

Here we present the results of our resolution study. For the single BH, no-cooling and BHBH equal mass, no-cooling cases we use the three resolutions (see Table II).

In the single BH-case the average accretion rate varies little with resolution (see left panel in Fig. 5). The maximum fractional difference of the mean accretion rate between different resolutions is 15%. Other quantities show a similar behavior. These results indicate that the resolutions used in this case are high enough for the main MRI effects to be captured and the results to be qualitatively independent of resolution. However, the resolution is not sufficiently high to perform a formal convergence test.

For the equal-mass case we observe a different behavior. The mean accretion rates appear to converge (see right panel in Fig. 5), but the low resolution run underestimates the accretion rate by almost a factor of 2, while the medium and high resolution runs are in good agreement. For the latter resolutions mean accretion rates agree to within 9%. We conclude that for the $q = 1$ case our adopted medium and high resolutions are sufficient for drawing qualitative conclusions and that higher resolutions are necessary for accurate quantitative results that reside in the convergent regime.

The results of the resolution study in the $q = 0$ and $q = 1$ cases differ because of the distribution of matter in both cases and our grid setup. In the $q = 0$ case there is more matter close to the BH, where very high resolution refinement levels reside, whereas in the $q = 1$ case the bulk of the matter remains outside the inner edge of the disk, where the grid resolution is not as high. As we show later, this is not the case in our $q < 1$ models. There, more matter resides closer to the BHs, and hence closer to the high resolution levels.

Based on our resolution study we conclude that the low resolution used in the equal-mass case is not sufficiently high to yield reliable results, but for the other mass ratios we consider in this work, our adopted low resolution suffices for a qualitative discussion. Thus, in the equal-mass cases results will be reported mainly from our medium resolution runs.

We stress here that these simulations, which include all relativistic effects and resolve the BHs, are computationally very demanding (see Sec. III) and increasing the resolution even further will incur a very large computa-

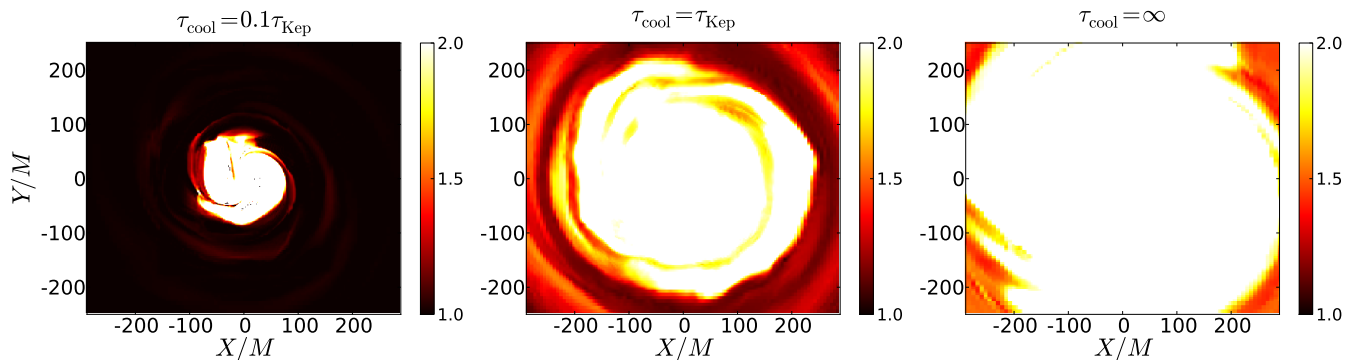


FIG. 4. K/K_0 for three $q = 1$ runs with different τ_{cool} at $t = 7700M$. Left panel: $\tau_{\text{cool}} = 0.1\tau_{\text{Kep}}$. Middle panel: $\tau_{\text{cool}} = \tau_{\text{Kep}}$. Right panel: No-cooling ($\tau_{\text{cool}} = \infty$). Cooling in the $\tau_{\text{cool}} = \tau_{\text{Kep}}$ case cannot keep up with heating, causing K to drift away from its initial value. Values much smaller than τ_{Kep} are required for rapid cooling. Steady state is not achieved in the $\tau_{\text{cool}} \geq \tau_{\text{Kep}}$ cases.

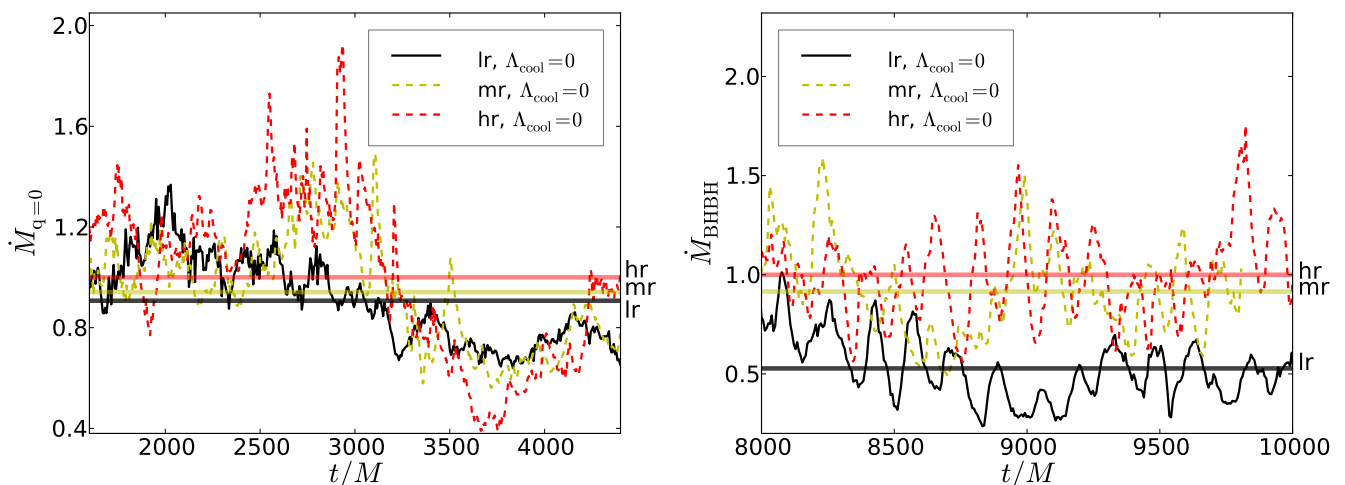


FIG. 5. Left panel: rest-mass accretion rate vs time for the $q = 0$ no-cooling cases at low (lr), medium (mr), and high (hr) resolutions. Right panel: rest-mass accretion rate vs time for the $q = 1$ no-cooling cases at low, medium, and high resolutions. The accretion rate in the $q = 0$ ($q = 1$) case is normalized by the mean accretion of the high resolution $q = 0$ ($q = 1$) run. The horizontal lines indicate the mean accretion rate at low, medium and high resolution.

tional cost. With increasing computer power and larger computer allocations we plan to improve our results in the near future.

B. Significance of B-fields

Previous hydrodynamic simulations and (semi)analytic models of circumbinary accretion disks using the simplified α -disk model (e.g. [59, 63]) showed that the main feature in the equal-mass *binary* case is that the density inside and near the binary’s orbit remains substantially lower than in the single BH case (see, e.g., Fig. 6). Such an inner cavity or “hollow” can have important consequences for the emergent radiation, such as line emission due to small optical depth and small bolometric luminosity from the hollow. Any such

difference between single BH vs. circumbinary accretion disks can provide a path to distinguishing a binary AGN versus a classical, standard (single BH) AGN [132]. The explanation for the existence of a hollow is that the binary tidal torques for $q \gtrsim 0.01$, are strong enough to push most matter away from the binary orbit [3]. The effect is most prominent in geometrically thin disks, which arise when radiative cooling is highly efficient.

However, even in the absence of viscosity or magnetic fields, the time-dependent tidal field strips off matter from the inner disk edge, giving rise to an accretion pattern consisting of two streams which penetrate the inner cavity and extend to the horizons of the BHs [3, 47, 73–75, 95].

Furthermore, recent MHD simulations [71, 72, 76] universally revealed that the reduction of density inside the cavity in the binary case is not as substantial as previ-

ously thought. Such simulations explore regimes in which the disk is geometrically thick, which partially accounts for the difference.

Here we present a comparison between magnetized and unmagnetized circumbinary accretion disks onto an equal mass BHBH, while all other physical and numerical parameters remain identical, to illustrate the importance of magnetic fields in filling the hollow with dense material.

1. Midplane-density

Figure 6 demonstrates the striking differences between no-cooling evolutions with and without magnetic fields at the same integration time. Magnetic-free hydrodynamic evolutions severely underestimate both the density in the inner regions and the overdensity due to the spiral arms. This indicates that the amount of matter stripped off by tidal torques is small compared to the amount of matter flowing into the hollow due to MHD turbulence.

2. Σ -profiles, $q = 1$

Next we compare the surface density profiles of magnetized vs unmagnetized disks. We find different profiles between the two cases as shown in Fig. 7. The $B = 0$ model remains relatively close to the initial data, apart from a slow, mild expansion due to tidal heating and shocks. When magnetic fields are present, the final disk profile is completely different from the initial data even though the binary torques are identical. This implies that the MRI-driven viscous torques have a much larger impact on the global disk structure than the binary tidal torques, except perhaps near the inner disk edge.

3. Sensitivity to cooling

We find a fundamental difference between $B = 0$ and $B \neq 0$ evolutions regarding their sensitivity to cooling. In the $B = 0$ case both $\Lambda \neq 0$ and $\Lambda = 0$ evolutions lead to essentially the same Σ -profile (see Fig. 7). This is in stark contrast to the $B \neq 0$ (magnetized) cases shown in Fig. 7, for which cooling has a strong impact, leading to a matter pile-up near the inner disk edge. As our particular choice of Λ serves to dissipate heat from shocks, we conclude that magnetic fields lead to far stronger shock heating in the disk than the binary tidal torques.

4. Accretion rate

The ratio of the time-averaged accretion rate without magnetic fields to that with magnetic fields is $\langle \dot{M}_{BHBH, B=0} \rangle / \langle \dot{M}_{BHBH, B \neq 0} \rangle \lesssim 1\%$ (see also Sec. V C). This result applies to both cooling and no-cooling cases.

In summary, $B = 0$ evolutions underestimate the material inside the cavity and accretion rates *by orders of magnitude*. Hence, incorporating magnetic fields is paramount for a proper treatment of circumbinary accretion disks.

C. Trend with mass ratio, $B \neq 0$

In this section we discuss the dependence of our multiple diagnostics on the binary mass ratio for our $B \neq 0$ cases. We use results from the single non-spinning BH case ($q = 0$) to normalize and compare our results for the binary cases.

1. Disk structure in the bulk and inside the cavity

We begin this section by discussing the qualitative evolution of the disk rest-mass density ρ_0 . For $q \neq 0$, the early evolution is similar for the different mass ratios, but departs strongly in the subsequent evolution depending on q . The onset of accretion occurs through two spiral streams, which remain attached to the horizons throughout the evolution, as shown in Figs. 8–15. Here we plot the rest-mass density contours in the equatorial plane. These streams are among the densest structures of the accretion flow, especially for the lowest non-zero mass ratio case $q = 0.1$ (see Figs. 14 and 15). Spiral density waves are launched near the inner edge of the disk, which propagate and dissipate into the outer disk. This feature can also be seen in Figs. 8–15 for all mass ratios.

Late in the evolution we find that when $q \neq 0$, the density of the matter inside the “cavity” in $\Lambda = 0$ cases is larger than that in $\Lambda \neq 0$ cases (see Figs. 8 and 9). Hence, the amount of matter in the hollow is smaller when we allow rapid cooling. This dependence on cooling arises because of the larger disk thickness in the no-cooling cases, which leads to a reduction in tidal torques [5, 133] near the binary orbit, allowing matter to overflow more easily.

We also find that the smaller the mass ratio the more matter pours into the cavity. This is anticipated from the Newtonian expression for the binary tidal torque [5, 133], which decreases with decreasing q . As expected, the largest contrast arises between the $q = 1$ and $q = 0$ cases, which becomes obvious by simply inspecting the rest-mass density contours in the equatorial plane as shown in Fig. 16. One can see the main difference: The presence of a region of lowered density with two accretion streams near the BHs in the binary $q = 1$ case – the “hollow” (or “cavity”) – and the absence of these features in the $q = 0$ case (left panel).

The relaxed disk structure in the precoupling regime is not axisymmetric. The back-sloshing of material towards the inner disk edge occurs mainly in two opposing directions and leads to a gradual overdense feature in the disk, which has been referred to as a “lump” [71, 72], and

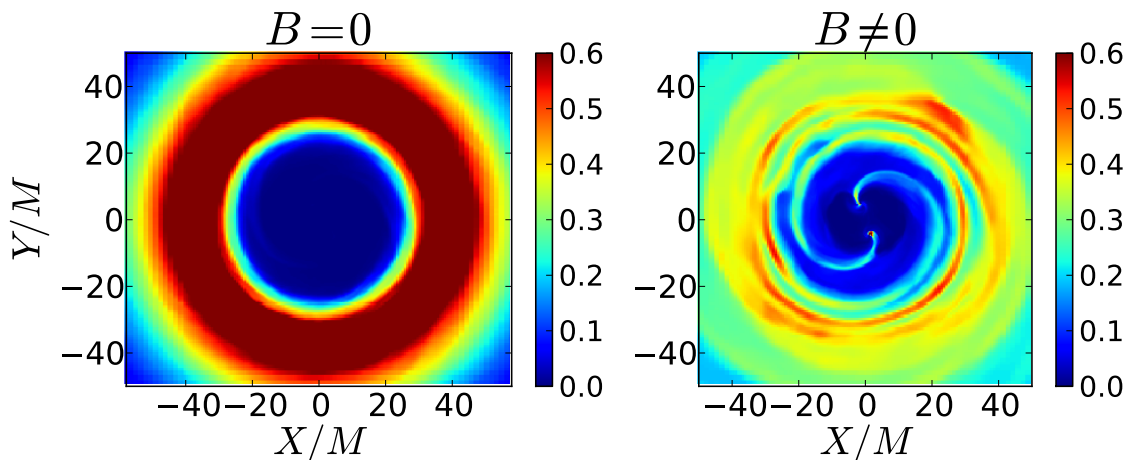


FIG. 6. Contours of rest-mass density normalized to the initial maximum rest-mass density in the equatorial plane at $t \sim 5000M$ for two $q = 1$ no-cooling cases. Left panel: $B = 0$. Right panel: $B \neq 0$. Notice the higher densities in spiral arms in the inner regions in the $B \neq 0$ case.

its presence has been linked with a growth in disk eccentricity (see also [63]). The nonaxisymmetric feature is stronger for models with cooling. Hence, a more realistic calculation with radiative transfer is necessary to assess the strength of nonaxisymmetric structure in a circumbinary disk.

As expected, the rest-mass density contrast between the two accretion streams becomes larger with smaller

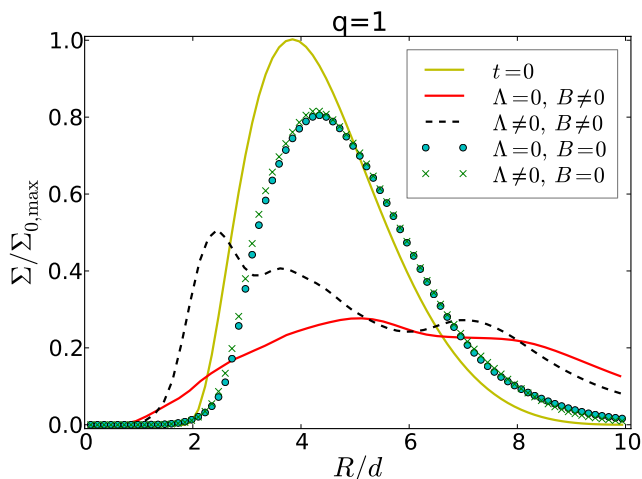


FIG. 7. Surface density profiles for several $q = 1$ cases: Initial profile (yellow, solid line), $B = 0$ no-cooling (green circles) & cooling (green crosses), $B \neq 0$ no-cooling (red, solid line) & cooling (black, dashed line) cases. Apart from the initial profile all other profiles are orbit-averaged over the last 10 orbits of evolution, beyond which the profile does not change appreciably. Notice the clear emergence of a pile-up near the inner disk edge in the cooling $B \neq 0$ case, as well as the relatively small change relative to the initial data in the $B = 0$ cases, and the similarity between $\Lambda = 0$ and $\Lambda \neq 0$ unmagnetized cases.

mass ratios. This effect is easily seen when comparing the rest mass density contours in the equatorial plane for $q = 0.25$, $q = 0.125$ and $q = 0.1$ cases (see Figs. 12 and 15).

In the $q = 1$ and 0.5 no-cooling cases we observe time variations in the density of the streams relative to each other: for about half an orbit one stream is stronger than the other.

We find that the supply of material channeled onto the BHs is sufficient to keep the BHs immersed in a persistent gaseous environment with $b^2/\rho_0 \sim 10^{-3}$. This means that the force-free electrodynamics approximation may be inadequate to globally describe the systems considered here.

For $q = 0.1$ there is hardly a low-density hollow (see Fig. 14). This is also revealed by the inner disk edge being close to or inside the orbit of the secondary, especially in the no-cooling case. In the $q = 0$ limit no hollow appears, as expected. However, we observe a region of lowered surface density near and inside the ISCO of the primary BH.

2. Inner disk edge

In Newtonian 2D studies of geometrically thin disks and large binary separations, the location of the inner disk edge is found to be roughly twice the binary separation, independent of q ; see, e.g., Table I in [59]. For the geometrically thick disks and binary separations we are considering, we find the inner disk edge in the relaxed state to be dependent on q and whether cooling is enabled.

In all cases (see the snapshots in Figs. 8–15), the inner disk edge is closer than predicted by Newtonian thin-disk calculations [59, 63, 71]. In the equal-mass cooling case the inner edge remains closer to the initial one (see

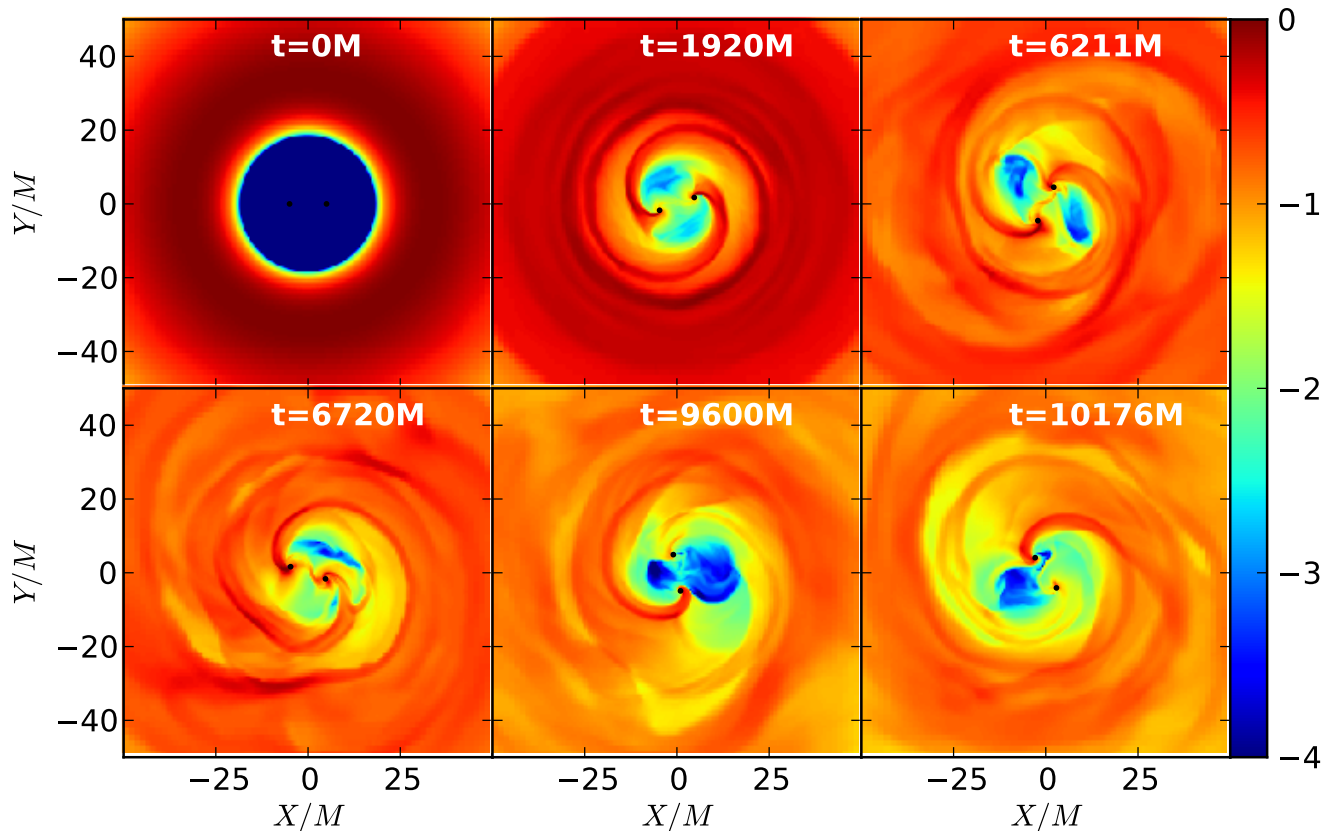


FIG. 8. Contours at select times of rest-mass density normalized to the initial maximum ρ_{\max} (log scale) in the equatorial plane. The plot corresponds to the $q = 1$ no-cooling case. Here $\rho_{\max} \simeq 5.6 \times 10^{-11} \left(\frac{\dot{M}_{\text{BHBH}}}{10M_{\odot} \text{ yr}^{-1}} \right) \left(\frac{M}{10^8 M_{\odot}} \right)^{-2} \text{ g cm}^{-3}$.

Fig. 7). The trend is such that the smaller the mass ratio the closer the disk edge is to the binary orbit. In the $q = 0.1$ no-cooling case the inner disk edge effectively coincides with the orbit of the secondary. We report the value for r_{in} found in each case in Table III, and plot r_{in} vs q in Fig. 17.

3. Surface density

In Fig. 18 we show the surface density (Σ) profiles of the relaxed disks, averaged over the last 10 binary orbital periods (for all mass ratios, cooling- and no-cooling). For all cases the relaxed state deviates strongly from the initial profile, highlighting the importance of evolving the system for at least a viscous time scale t_{vis} at the radii of interest, where

$$\frac{t_{\text{vis}}}{M} \equiv \frac{2R^2}{3\nu M} = 8485 \left(\frac{\alpha}{0.1} \right)^{-1} \left(\frac{H/R}{0.3} \right)^{-2} \left(\frac{R}{18M} \right)^{3/2}, \quad (11)$$

and where $\nu \equiv 2\alpha P/3\rho_0\Omega_{\text{Kep}}$ is the shear viscosity, with $\Omega_{\text{Kep}} = (M/R^3)^{1/2}$.

No-cooling: The evolutions for $q = 1$ and 0.5 are similar in terms of their Σ profiles. The other cases ($q = 0.25 - 0$) yield similar Σ which extend further in than for $q = 1$ and 0.5. The surface density diagnostic clearly demonstrates that the Newtonian thin-disk feature that the cavity edge is at twice the binary separation and independent of the mass ratio does not hold in this class of runs.

Cooling: For non-zero mass ratios, cooling yields a pile up of dense gas near the inner disk edge, which is absent in the no-cooling runs and is strongest for the equal-mass case. Apart from the pile-up at small radii, all evolutions have a rather similar profile at larger radii. In the cooling cases the cavity edge is farther out than for no-cooling, but still closer than twice the binary separation. The dependence on mass ratio is weaker than in the no-cooling cases, but still in some disagreement with the Newtonian thin-disk calculations.

4. Effective α -stress

Figure 19 shows the averaged effective Shakura-Sunyaev α parameter profiles for all mass ratios, both

TABLE III. Table summarizing our main results. Columns show case label, inner disk edge normalized to the binary separation r_{in}/d , the mean accretion rate and its approximate standard deviation normalized to the no-cooling single BH mean accretion rate ($\langle \dot{M}_{\text{BHBH}} \rangle \pm \delta \dot{M}_{\text{BHBH}} / \langle \dot{M}_{q=0} \rangle$), main Fourier frequencies normalized by the binary orbital period in the Fourier analysis of the accretion rate, Shakura-Sunyaev α -parameter^a, the mean Poynting luminosity $\langle L_{\text{EM}} \rangle$, and the mean cooling luminosity $\langle L_{\text{cool}} \rangle$ both normalized to the binary mean accretion rate. A dash “–” indicates “no information available”.

Case	r_{in}/d	$(\langle \dot{M}_{\text{BHBH}} \rangle \pm \delta \dot{M}_{\text{BHBH}}) / \langle \dot{M}_{q=0} \rangle$	f/f_{orb}	α	$\langle L_{\text{EM}} \rangle / \langle \dot{M}_{\text{BHBH}} \rangle c^2$	$\langle L_{\text{cool}} \rangle / \langle \dot{M}_{\text{BHBH}} \rangle c^2$
1:1nc-mr	0.89	$0.43 \pm 50\%$	(1.0, 1.5)	0.04	0.013	–
1:2nc-lr	1.33	$0.24 \pm 60\%$	(0.7, 1.5)	0.05	0.012	–
1:4nc-lr	1.24	$0.36 \pm 20\%$	(0.7, 1.5)	0.03 – 0.1	0.010	–
1:8nc-lr	1.06	$0.41 \pm 40\%$	0.7	0.03 – 0.06	0.010	–
1:10nc-lr	0.92	$0.50 \pm 50\%$	–	0.07	0.017	–
0nc-hr	0.32 ^b	$1.00 \pm 24\%$	–	0.05	0.011	–
1:1c-mr	1.48	$0.43 \pm 60\%$	(0.5, 1.5)	0.2	0.004	0.127
1:2c-lr	1.65	$0.36 \pm 30\%$	1.0	0.12	0.003	0.110
1:4c-lr	1.57	$0.32 \pm 60\%$	1.0	0.1	0.002	0.107
1:8c-lr	1.46	$0.31 \pm 30\%$	0.6	0.08	0.006	0.096
1:10c-lr	1.36	$0.43 \pm 30\%$	–	0.013	0.006	0.081
0c-lr	0.39	$0.62 \pm 10\%$	–	0.012	0.002	0.115

^a In some cases we quote a range of values because a single radially averaged value would overestimate α .

^b For ease of comparison, in the single BH case we normalize r_{in} to $10M$ even though it does not correspond to an orbital separation.

for cooling and no-cooling models in the relaxed state. The average is taken over the last 10 binary orbits. In Table III we also quote characteristic α values obtained by additionally averaging over radii from the inner disk edge out to the location of the density maximum. We plot α vs q in Fig. 17.

In all cases we observe larger values for α in the cooling cases than for the no-cooling cases, and there is always a steep increase in α -stress at smaller radii. For the $q = 1$ cooling case we find $\alpha(r_{in} < r < r_{\text{max}}) \sim 0.2$ and $\alpha(r_{in} < r < r_{\text{max}}) \sim 0.1$ for all other cooling cases. A typical value for all no-cooling cases is $\alpha(r_{in} < r < r_{\text{max}}) \sim 0.05$. The higher stress for cooling cases results from the additional gas compression and associated amplification of magnetic fields when cooling is allowed.

5. Accretion rates

We compute the accretion rates through the individual BHs as well as the total accretion rate onto the binary, and normalize these by the (time-averaged) single, non-spinning BH accretion rate.

For a given maximum rest-mass density and total BH mass, we find the highest accretion rate in the single BH case. This is consistent with the expectation that the absence of a tidal-torque barrier will allow matter to flow more easily toward the BH(s).

By contrast, the tidal torque is maximized for $q = 1$ (all else being equal), so the expectation is that the accretion rate will be minimum for $q = 1$. In agreement with this expectation we find the accretion rate in the $q = 1$ cases to be smaller than all other mass ratios we consider here.

In Table III we list the average accretion rate vs mass

ratio, and plot the results in Fig. 17. The general trend is that lower mass ratios have higher accretion rates. In the $q = 0.1$ case the average accretion rate is about 50% that of the single BH case with the same initial maximum rest-mass density and total BHBH mass, while the average accretion rate in the equal-mass case is roughly 33% of that in the $q = 0$ case.

For $q = 1$ and 0.5 both black holes accrete at comparable rates whether cooling is applied or not (see four upper rows, left panels Fig. 20). However, we observe that often the accretion rates on the individual BHs are anti-phased, i.e., accretion occurs for half an orbit primarily on one BH and then for the second half of the orbit on the other BH. This behavior in the relaxed state is due to an “alternating” pattern in which denser material primarily plunges first through one stream and then through the other.

In Fig. 20 we also plot the accretion rates for $q = 0.25$ and 0.1 , with and without cooling (three lower rows, left panels). It is apparent that for $q = 0.25$ the accretion rate onto the primary is comparable to that onto the secondary when $\Lambda = 0$. However, when $\Lambda \neq 0$ the dominant contribution to the total accretion rate comes from the primary. In the $q = 0.1$ case we observe that the dominant contribution to the total accretion rate comes from the primary whether cooling is applied or not, and the same holds true for the $q = 0.125$ case.

This result in the $q = 0.1$ case can be qualitatively understood through a rough analogy to Bondi-Hoyle-Lyttleton accretion: The secondary has a smaller mass and moves faster on its orbit reducing its effective capture cross section as suggested by Bondi-Hoyle-Lyttleton accretion (see e.g. [47]). Also the surface area of the secondary is roughly a factor $M_{\text{BH}}^2/m_{\text{bh}}^2 \sim 100$ smaller than

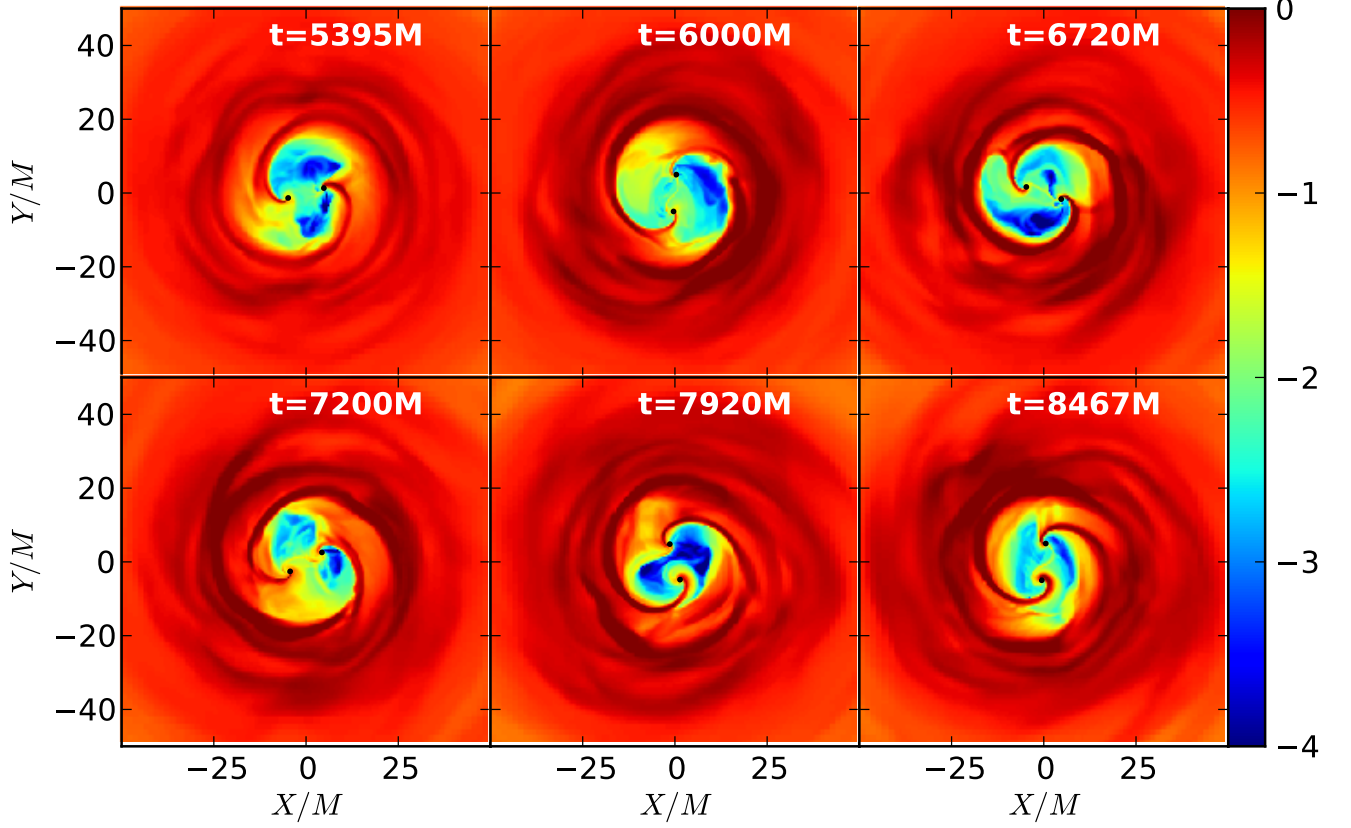


FIG. 9. Contours at select times of rest-mass density normalized to the initial maximum ρ_{\max} (log scale) in the equatorial plane. The plot corresponds to the $q = 1$ cooling case. Here $\rho_{\max} \simeq 2.1 \times 10^{-11} \left(\frac{\dot{M}}{1.75 M_{\odot}/\text{yr}} \right) \left(\frac{M}{10^8 M_{\odot}} \right)^{-2} \text{ g cm}^{-3} \simeq 2.1 \times 10^{-11} \left(\frac{L_b}{L_{\text{Edd}}} \right) \left(\frac{M}{10^8 M_{\odot}} \right)^{-1} \text{ g cm}^{-3}$.

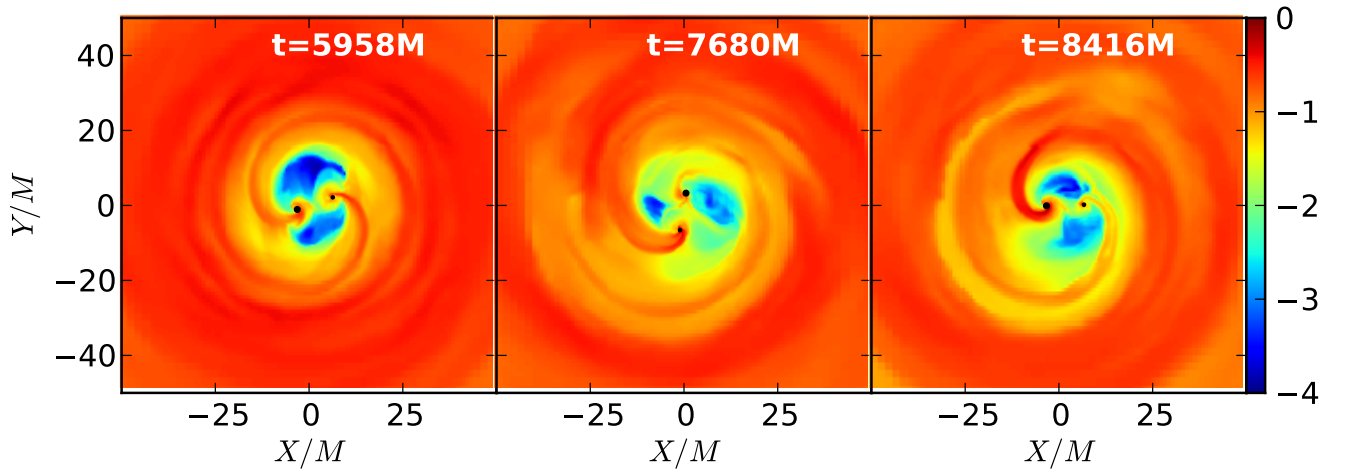


FIG. 10. Contours at select times of rest-mass density normalized to the initial maximum ρ_{\max} (log scale) in the equatorial plane. The plot corresponds to the $q = 0.5$ no-cooling case. Here $\rho_{\max} \simeq 8.3 \times 10^{-11} \left(\frac{\dot{M}_{\text{BHH}}}{15.8 M_{\odot} \text{ yr}^{-1}} \right) \left(\frac{M}{10^8 M_{\odot}} \right)^{-2} \text{ g cm}^{-3}$.

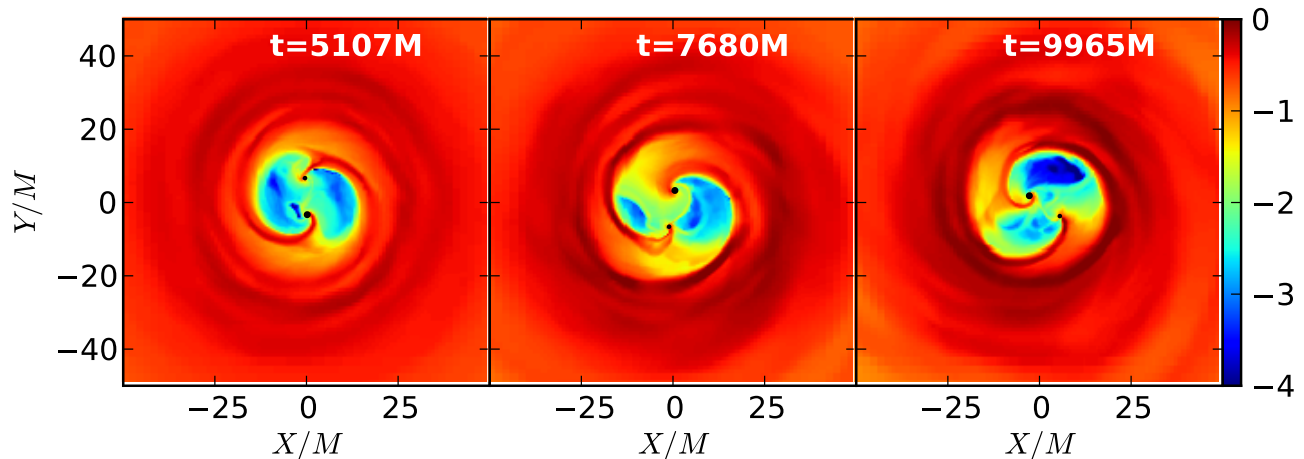


FIG. 11. Contours at select times of rest-mass density normalized to the initial maximum ρ_{\max} (log scale) in the equatorial plane. The plot corresponds to the $q = 0.5$ cooling case. Here $\rho_{\max} \simeq 4.2 \times 10^{-11} \left(\frac{\dot{M}}{2.85 M_{\odot}/\text{yr}} \right) \left(\frac{M}{10^8 M_{\odot}} \right)^{-2} \text{ g cm}^{-3} \simeq 4.2 \times 10^{-11} \left(\frac{L_b}{L_{\text{Edd}}} \right) \left(\frac{M}{10^8 M_{\odot}} \right)^{-1} \text{ g cm}^{-3}$.

that of the primary. Note however, that the secondary plays a role in stripping matter off the inner disk edge effectively as it orbits closest to (or even through) the disk, so the accretion rate onto the secondary is not generally expected to be 100 times smaller than the accretion rate onto the primary.

In particular, in the $q = 0.1$ no-cooling case a dense persistent structure co-orbits with the secondary (see Fig. 14). The density in this structure exceeds the density of matter near the primary by more than a factor of two.

6. Variability

We now report results from the Fourier analysis of the accretion rate. These can be seen in the right panels of Fig. 20. A summary of the primary Fourier modes for the different cases is presented in Table III.

In the $q = 1$ case a Fourier analysis of \dot{M}_{BH} (accretion rate onto the primary) and \dot{m}_{bh} (accretion rate onto the secondary) reveals a characteristic frequency near $(2/3)M\Omega_{\text{BHBH}}$, in agreement with [76]. The analysis of \dot{M}_{BHBH} (the total *binary* accretion rate) gives a dominant Fourier mode with a frequency twice as high. We observe a peak at the binary period only for $q = 0.5$ and 0.25 , and only for the cooling cases (see Fig. 20). These results indicate that if the variability in the accretion rate is directly translated into a variability of EM signatures, inferring the binary frequency from EM observations may not be straightforward. We observe variability for other mass ratios as well. The frequencies for the equal mass case also appear in other cases, in addition to other weaker contributions, but a clear trend is not evident. The most prominent and clean periodic sig-

nature occurs in the $q = 0.5$ no-cooling case (see Fig. 20 and discussion in [64]). Other strong Fourier modes are observed in $q = 0.5$ cooling and the $q = 0.25$ cases. For $q = 0.125$ and $q = 0.1$ no significant periodicities are observed.

In the $q = 0.1$ case the variability is dominated by variations in the accretion flow onto the primary. The Fourier analysis yields rather irregular accretion, i.e. not very pronounced frequencies. The secondary accretes at several pronounced frequencies, but the amplitude of the variations is much smaller.

In [64, 65] the dependence on q of the variability was studied for geometrically thin (“locally isothermal” disks) and proposed as a key feature to observationally distinguish accreting BHBHs from standard, single BH AGNs. In our Fourier analysis the individual peaks are less significant than in [64, 65] and the Fourier spectrum yields a more complex structure. This discrepancy is likely due to a combination of additional effects including differences in the viscosity prescription (i.e. MHD turbulence vs. α -viscosity), cooling prescriptions, thin vs. thick disks, 2D vs 3D, and the EOS. These differences result in geometrically thin vs thick disks, which are seen to have different variability.

7. Luminosities

We compute the cooling (L_{cool}) and Poynting (L_{EM}) luminosities, as well as the energy loss rate due to outflowing matter (L_{gas}) for all cases. We typically find L_{gas} is comparable to L_{EM} and quite smaller than L_{cool} . We highlight representative cases and summarize all values for the different q characterizing the relaxed state in Table III.

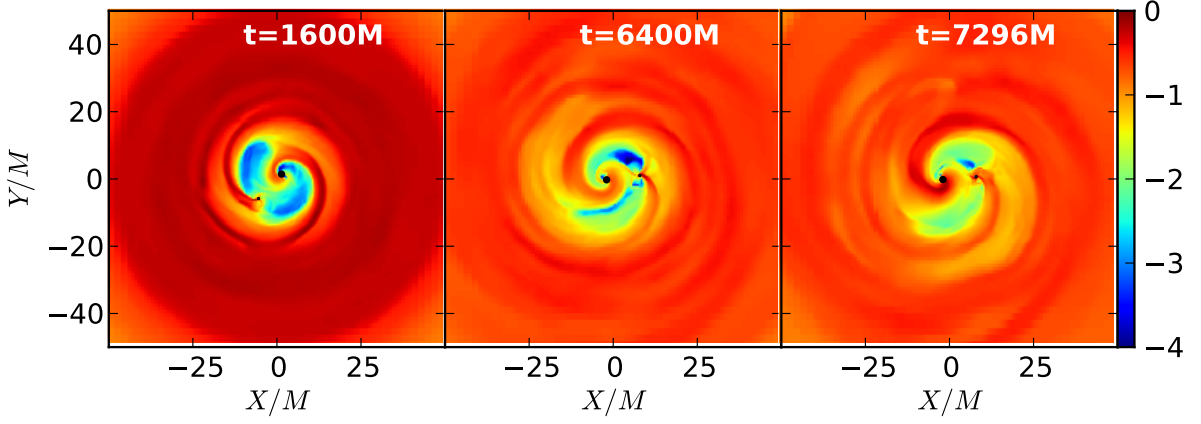


FIG. 12. Contours at select times of rest-mass density normalized to the initial maximum ρ_{\max} (log scale) in the equatorial plane. The plot corresponds to the $q = 0.25$ no-cooling case. Here $\rho_{\max} \simeq 6.7 \times 10^{-11} \left(\frac{\dot{M}_{\text{BHBH}}}{13M_{\odot} \text{ yr}^{-1}} \right) \left(\frac{M}{10^8 M_{\odot}} \right)^{-2} \text{ g cm}^{-3}$.

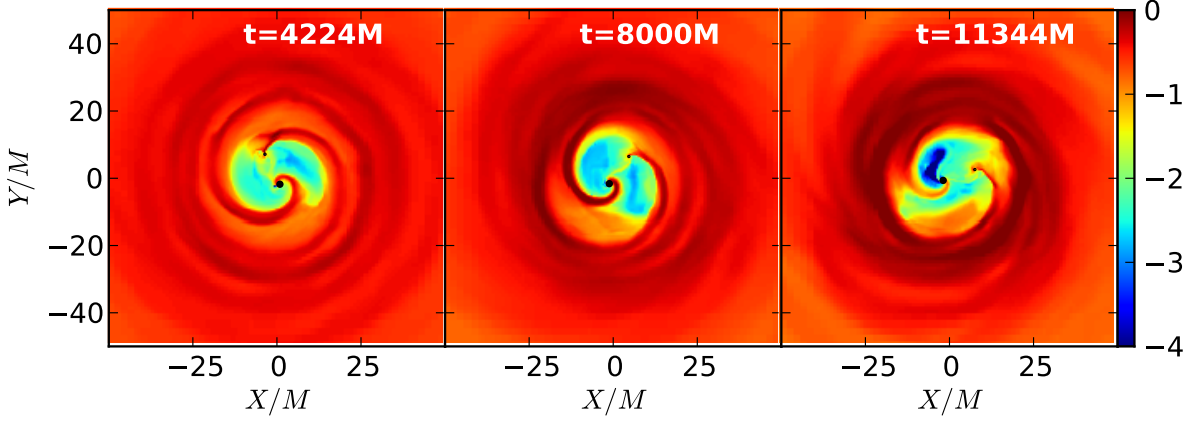


FIG. 13. Contours at select times of rest-mass density normalized to the initial maximum ρ_{\max} (log scale) in the equatorial plane. The plot corresponds to the $q = 0.25$ cooling case. Here $\rho_{\max} \simeq 3.75 \times 10^{-11} \left(\frac{\dot{M}}{2.27M_{\odot}/\text{yr}} \right) \left(\frac{M}{10^8 M_{\odot}} \right)^{-2} \text{ g cm}^{-3} \simeq 3.75 \times 10^{-11} \left(\frac{L_{\text{b}}}{L_{\text{Edd}}} \right) \left(\frac{M}{10^8 M_{\odot}} \right)^{-1} \text{ g cm}^{-3}$.

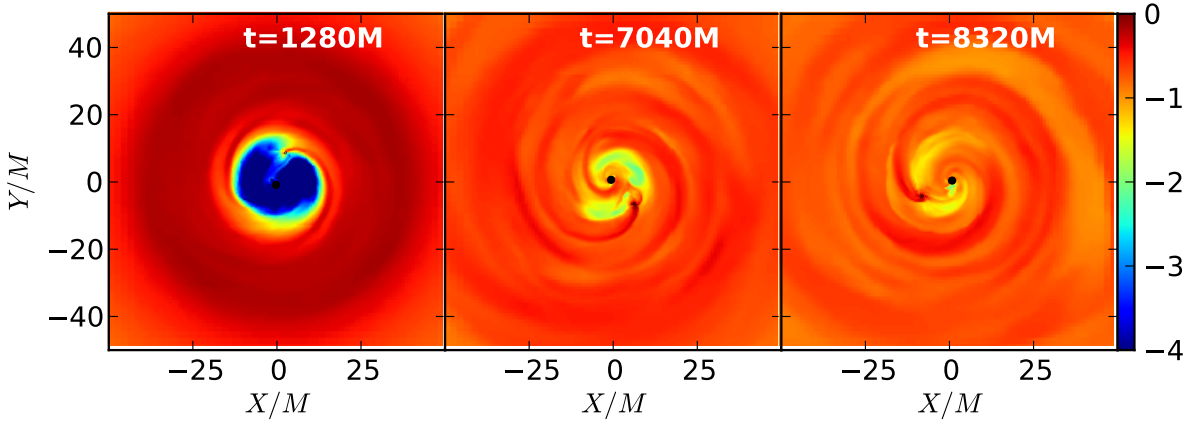


FIG. 14. Contours at select times of rest-mass density normalized to the initial maximum ρ_{\max} (log scale) in the equatorial plane. The plot corresponds to the $q = 0.1$ no-cooling case. Here $\rho_{\max} \simeq 6 \times 10^{-11} \left(\frac{\dot{M}_{\text{BHBH}}}{11M_{\odot} \text{ yr}^{-1}} \right) \left(\frac{M}{10^8 M_{\odot}} \right)^{-2} \text{ g cm}^{-3}$.

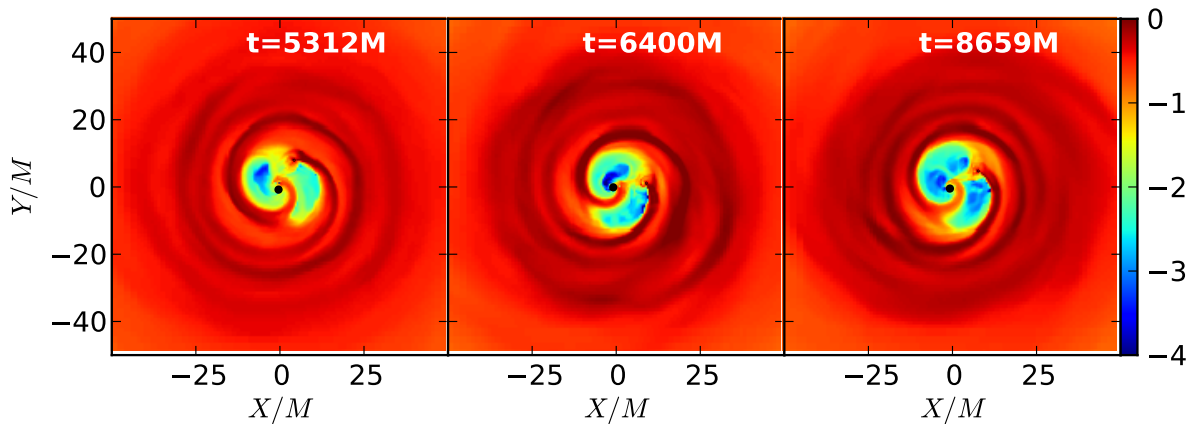


FIG. 15. Contours at select times of rest-mass density normalized to the initial maximum ρ_{\max} (log scale) in the equatorial plane. The plot corresponds to the $q = 0.1$ cooling case. Here $\rho_{\max} \simeq 3.5 \times 10^{-11} \left(\frac{\dot{M}}{2.85M_{\odot}/\text{yr}}\right) \left(\frac{M}{10^8 M_{\odot}}\right)^{-2} \text{ g cm}^{-3} \simeq 3.5 \times 10^{-11} \left(\frac{L_b}{L_{\text{Edd}}}\right) \left(\frac{M}{10^8 M_{\odot}}\right)^{-1} \text{ g cm}^{-3}$. The gas is denser everywhere compared to mass ratios closer to unity; compare to Figs. 8, 9, 10, 11, 12, 13.

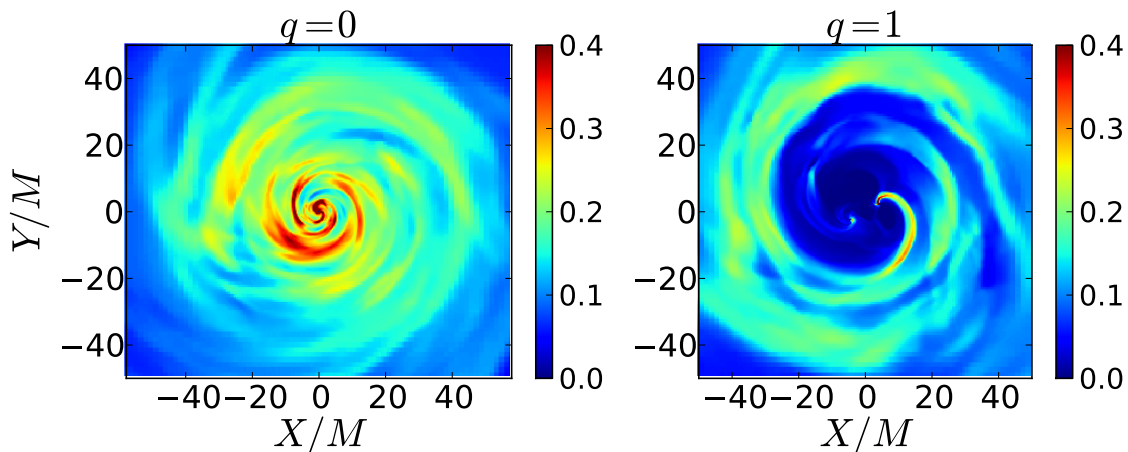


FIG. 16. Contours of rest-mass density (linear color scale) normalized to the initial maximum in the equatorial plane at $t = 10000M$. Left panel: $q = 0$ no-cooling. Right panel: $q = 1$ no-cooling case.

The large variability seen in the accretion rate is only partially reflected in the cooling luminosities and not reflected in the Poynting luminosities. However, these conclusions need to be confirmed with a self-consistent treatment involving radiative transfer.

In all cooling cases we find that the cooling luminosity is significantly larger than the Poynting luminosity and the energy loss rate due to outflowing matter by almost a factor of 10 (see Table III).

We estimate and compare the contributions to the cooling luminosity from various regions in the disk: the outer disk, the inner edge, and the cavity (see Fig. 21). We find that although the outer disk gives the largest contribution, the inner edge and cavity interior are a substantial portion ($\sim 30\%$) of the total cooling luminosity. Therefore, the activity in the cavity cannot be ignored,

as has been done in earlier studies.

8. Opacities

We estimate the Thompson scattering (τ_{es}) and free-free absorption (τ_{ff}) optical depths in all cases. We do not find a strong dependence of $\tau^* = (3\tau_{\text{es}}\tau_{\text{ff}})^{1/2}$, τ_{es} and τ_{ff} on the mass ratio. Our crude analysis shows $\tau^* \sim \mathcal{O}(1)(L_b/L_{\text{Edd}})^{9/16}(M/10^8 M_{\odot})^{-1/16}$ throughout the bulk of the disk. In conjunction with the radiation pressure dominance found for near Eddington accretion rates, this result justifies our choice of $\Gamma = 4/3$ for the bulk of the disk. Some cases are marginal, however given the crudeness of our estimate and scaling arguments the choice of adiabatic index is adequate. The

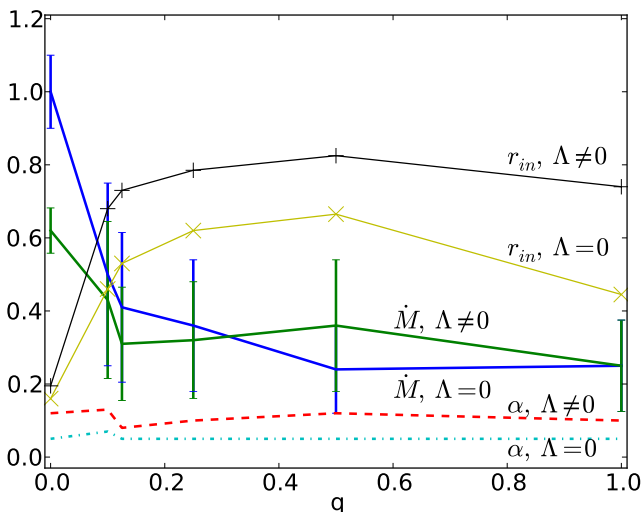


FIG. 17. Mean accretion rate \dot{M} (normalized to the no-cooling single BH accretion rate), α , and r_{in} (normalized to twice the binary separation) as functions of q for cooling and no-cooling cases (all at low resolution). In the absence of medium and high resolution runs for $q \neq 1$ we place error bars in \dot{M} based on the $q = 1$ resolution study. These error bars are chosen to be 50%, corresponding to the fractional difference between the high and low resolutions runs in the $q = 1$ case (see Sec. V A). The error bar in the $q = 0$ case is 15% corresponding to the fractional difference between the high and low resolutions runs in the $q = 0$ case.

dominant source of opacity in all cases is electron scattering. Within the cavity we find that outside the accretion streams the matter is optically thin. This means that radiation from the cavity can freely stream out, and it is likely that (depending on the local temperature) cyclotron lines may give rise to a nonthermal component to the emergent EM spectrum.

We find that τ^* is affected by cooling. The runs with cooling have larger τ^* than those without cooling.

9. Characteristic EM radiation frequencies

The characteristic effective temperatures [see Eq. (9)] are

$$T_{\text{eff}} \sim 10^5 \left(\frac{L_b}{L_{\text{Edd}}} \right)^{1/4} \left(\frac{M}{10^8 M_\odot} \right)^{-1/4} \text{ K.} \quad (12)$$

The corresponding characteristic thermal radiation frequencies ($\nu_{\text{bb}} \sim k_B T_{\text{eff}}/h$) are reduced by a redshift fac-

tor $1/(1+z)$, and are

$$\begin{aligned} \nu_{\text{bb}} &\sim 10^{15} \left(\frac{\varepsilon}{0.08} \right)^{1/4} \left(\frac{M}{10^8 M_\odot} \right)^{-1/2} \\ &\quad \left(\frac{\dot{M}}{2.25 M_\odot/\text{yr}} \right)^{1/4} (1+z)^{-1} \text{ Hz} \\ &\sim 10^{15} \left(\frac{M}{10^8 M_\odot} \right)^{-1/4} \left(\frac{L_b}{L_{\text{Edd}}} \right)^{1/4} (1+z)^{-1} \text{ Hz.} \end{aligned} \quad (13)$$

The lower limit to the equatorial temperature in the cavity for all cases (assuming $\rho_0 \epsilon = aT^4$) is

$$T \sim 10^5 \left(\frac{L_b}{L_{\text{Edd}}} \right)^{1/4} \left(\frac{M}{10^8 M_\odot} \right)^{-1/4} \text{ K,} \quad (14)$$

implying that the electrons are nonrelativistic, and hence they emit cyclotron and not synchrotron radiation. This result, too, should be confirmed with radiative transfer calculations. Typical cyclotron frequencies in the cavity then are

$$\nu_{\text{cy}} \sim 10^6 \left(\frac{M}{10^8 M_\odot} \right)^{-1/2} \left(\frac{L_b}{L_{\text{Edd}}} \right)^{1/2} (1+z)^{-1} \text{ Hz.} \quad (15)$$

Note that due to the large radiation pressure near the Eddington limit, one expects that any dust will be blown away from the disk and may accumulate at much larger radii than our computational domain. This dust is likely to absorb the optical/UV radiation and re-emit it in the IR [52, 134].

10. Outflows and jets

In Fig. 22 ($q = 0.1$ and 1 cases) we plot the ratio $b^2/(2\rho_0)$, which equals the terminal Lorentz factor in axisymmetric steady-state jet flows. Close to the BH, values approaching $b^2/(2\rho_0) \sim 20$ are common, dropping to $b^2/(2\rho_0) \sim 10$ at larger heights Z (in the funnel). We observe mildly relativistic outflows in all cases. Our 3D visualizations of the B-field lines (see Fig. 23) unambiguously show that there are field lines emanating from each BH horizon and extending into the polar regions. Near the BHs [$r \sim \mathcal{O}(10M)$] this leads to a dual jet structure that at larger radii [$r \sim \mathcal{O}(100M)$] merges into one common helical structure. Due to this effect the dual jets may not be detectable individually. In the context of force-free simulations around binary black holes, the existence of individually detectable dual jets was proposed in [80]. However, in [135] it was shown that while a dual-jet component is present, it is subdominant with respect to the predominantly quadrupolar EM emission, thereby casting tight constraints on the detectability of such dual jets. Regardless, the ‘‘cavity’’ contains a lot of dense matter so that the assumption of the force-free limit of ideal MHD may not be applicable. An MHD calculation can

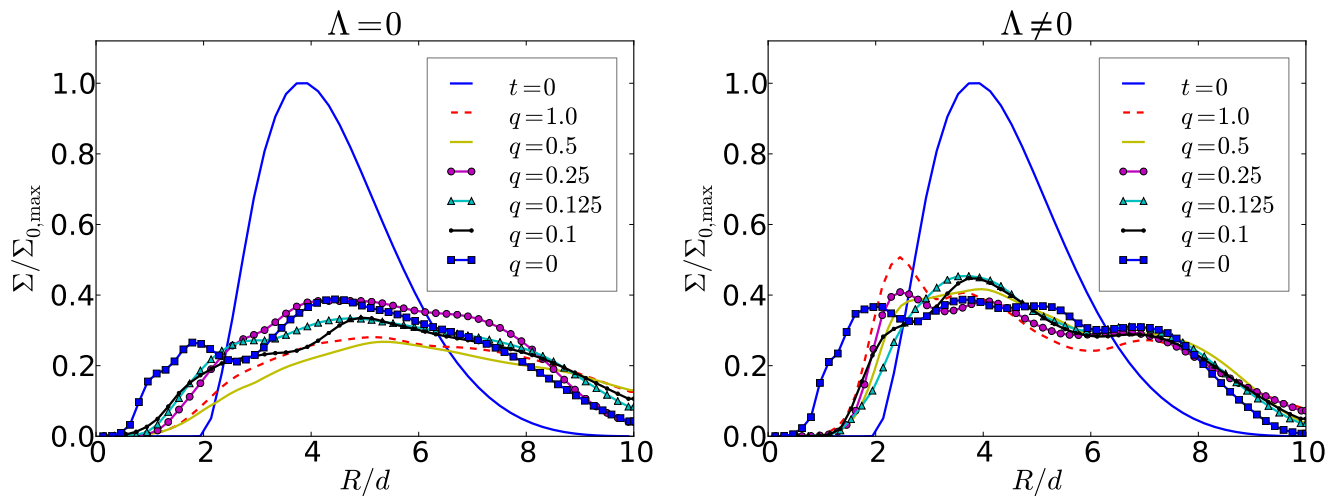


FIG. 18. Disk surface density Σ -profile for different mass ratios as a function of cylindrical radius (normalized to the binary separation $d \sim 10M$). Left panel: no-cooling cases. Right panel: cooling cases. Except for the initial profile all other curves correspond to the relaxed state averaged over the last 10 binary orbital periods. In all these $B \neq 0$ cases the relaxed profile deviates strongly from the initial one. In the $\Lambda = 0$ sequence the density reaches further toward small radii with decreasing q . In the $\Lambda \neq 0$ sequence, one can see the pile-up near the inner disk edge, which is strongest for large q .

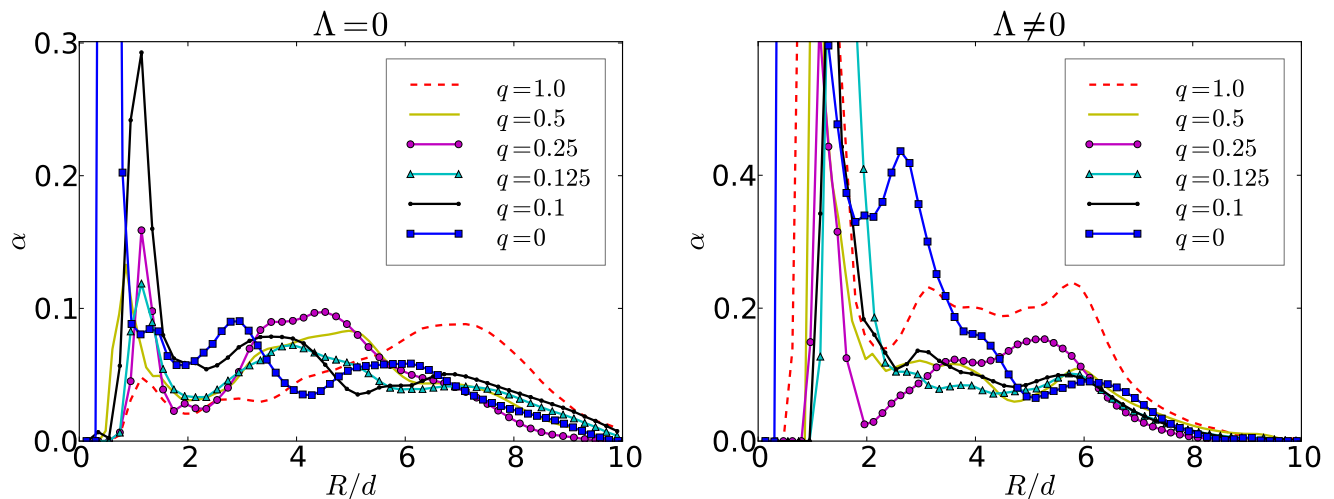


FIG. 19. Shakura-Sunyaev α profiles for all mass ratios. Left panel: no-cooling cases. Right panel: cooling cases. Profiles have been averaged over the last 10 binary orbital periods. Cooling cases tend to yield larger values. In all cases the stress increases inside the cavity.

resolve this question, and our results suggest that for twin jets to be detectable as individual jets, it may require either BH spins misaligned with the orbital angular momentum or tilted accretion disks [70]. Although for geometrically thin disks binary-disk misalignment may be unlikely [136], it may be possible for geometrically thick disks.

VI. CONCLUSIONS

We presented general relativistic magnetohydrodynamic simulations of magnetized circumbinary accretion

disks onto binary black holes with mass ratios ranging from 1:1 to 1:10. We model the disks using a Γ -law equation of state with $\Gamma = 4/3$ – appropriate for optically thick, thermal radiation pressure-dominated fluids. We focus on a disk near decoupling and perform our computations for $\sim 10000M$ (45 binary orbits). We compute the disk structure after the disk has reached a quasi-relaxed state. This dynamically quasi-steady state is a result of binary tidal torques balancing viscous torques arising from MHD turbulence triggered by the magnetorotational instability (MRI). The tidal and viscous torques heat the gas, which is expected to radiate and cool. To bracket this possibility we perform runs without cooling,

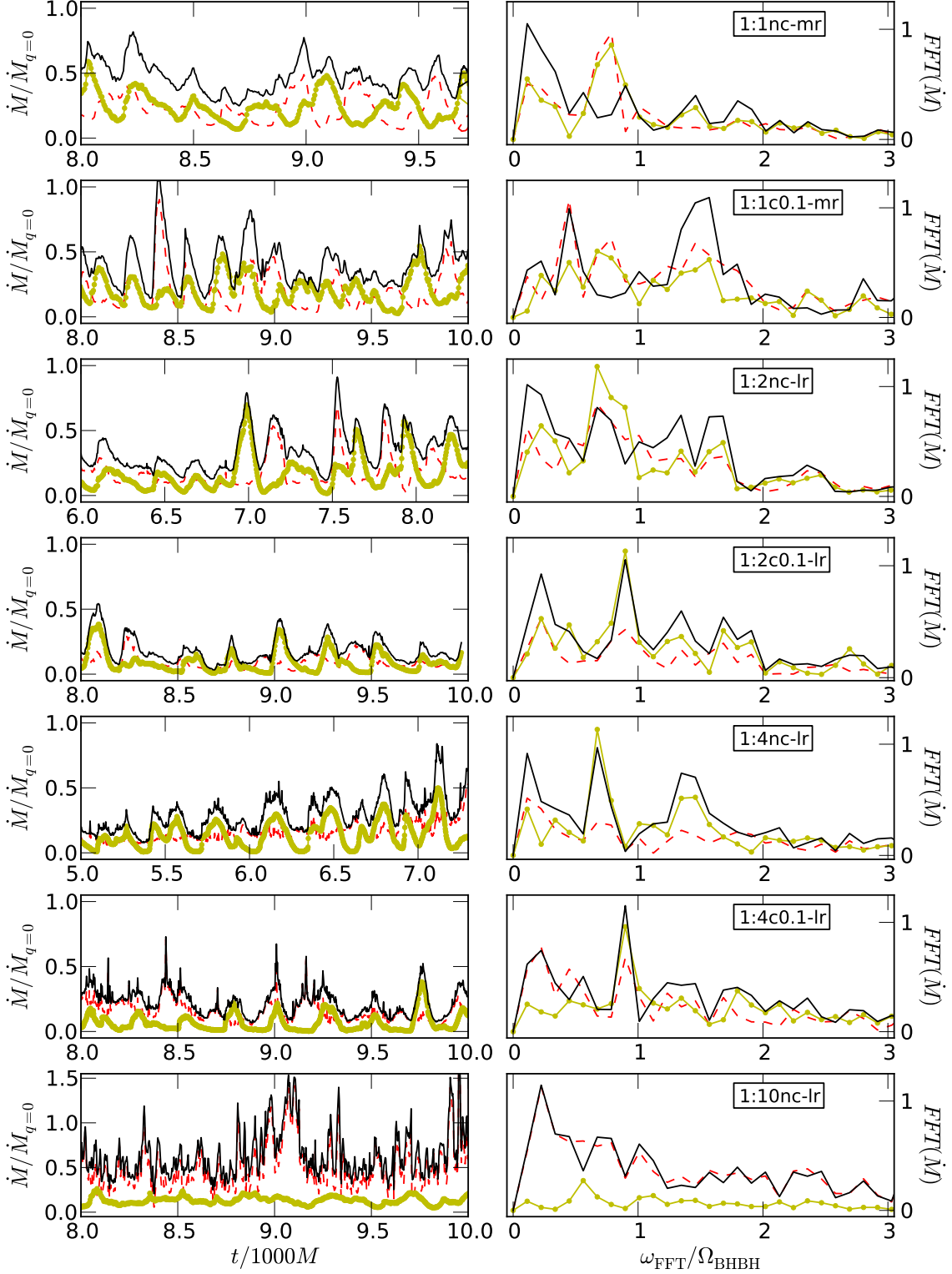


FIG. 20. Left panels: Late evolution of mass accretion rate onto the binary (solid, black lines), primary (red, dashed lines), and secondary (solid-dotted, yellow lines). Right panels: Fourier transform of the accretion rates shown on the left. From top to bottom we show the $q = 1$ cooling and no-cooling, $q = 0.5$ cooling and no-cooling, $q = 0.25$ cooling and no-cooling, and $q = 0.1$ no-cooling cases.

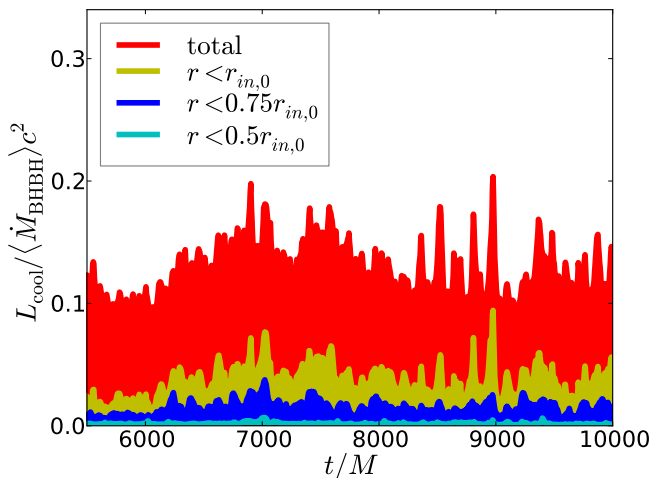


FIG. 21. Contribution to L_{cool} from the inner cavity and outer disk for the $q = 1$ cooling case. The notation $r < R_0$ means the cooling luminosity integral $\int_V \Lambda u_0 \sqrt{-g} d^3x$, where V is the volume within a coordinate sphere of radius R_0 . Note that about 30% of the total cooling luminosity arises within $r_{\text{in},0}$.

and runs with extremely rapid cooling, adopting an effective cooling prescription that resembles a leakage scheme.

We study how the structure of the accretion flow is altered for the five different mass ratios. We employ several diagnostics, including the accretion rate and its Fourier transform, estimates of the electromagnetic luminosity and the expected characteristic frequencies of the emergent electromagnetic radiation, to compare the cases.

In the equal mass case we find that simulations without magnetic fields underestimate the accretion rates, and adopting our cooling prescription, the total luminosity of the source by two orders of magnitude. This is due to a substantial increase of the amount of matter in the “cavity” when magnetic fields are present. We also conclude that magnetic fields alter the quasi-steady surface density profile. Turbulent B-fields lead to more shock heating than the binary tidal torques alone, thereby boosting cooling luminosities above the values found in unmagnetized disks.

The surface density profile of the disk is sensitive to the mass ratio mainly in the innermost regions. Cooling leads to a density enhancement near the inner disk edge (a pile-up) which is strongest in the equal mass case.

We find that for all mass ratios a two-stream accretion pattern is present. These streams are attached to the horizons, with the density close to the horizons being among the densest part of the accretion flow. In particular, for the $q = 0.1$ case the material overflows into the inner cavity and (partially) refills the hollow present in the initial data. During this process a persistent dense structure forms around the secondary. This behavior suggests that it would be inadequate to ignore the flow inside the cavity, which only simulations in full GR can treat

correctly.

The average binary accretion rates relative to the single, non-spinning BH case range from 50% ($q = 0.1$) to 24% ($q = 0.5$) with a general trend that the accretion rate becomes smaller as $q \rightarrow 1$. For $q = 0.5$ and $q = 1$, both BHs accrete at a comparable rate (on average), but for roughly half a binary period one of the two accretion streams is significantly stronger than the other, boosting the accretion rate onto one BH and diminishing that onto the other. For smaller q the accretion and variability is increasingly dominated by the primary BH, especially in the cases with cooling. For the single BH ($q = 0$) significant variability ceases. In general we do not observe evidence for variability exactly at the binary period. Two exceptional cases in which the binary frequency is detected are the $q = 0.5$ and 0.25 cooling models.

We find that the variability in the accretion rate is not reflected in the variability of either the Poynting or the cooling luminosity. We also find that our cooling luminosity is always larger than the Poynting luminosity, though careful GRMHD simulations with radiative transfer are necessary to confirm these findings.

The cavity radiates an amount comparable to the outer disk. Only the innermost regions reflect the strong variability seen in \dot{M} , but in general the radiation from the outer disk smears these variabilities out. We tentatively conclude that it will be challenging to distinguish between single BH and binary BH AGN sources, unless other effects such as binary disk misalignment are present. However, radiative transfer calculations are required to confirm this result.

We observe nonaxisymmetric structure in the relaxed disk. A “lump” forms near the inner disk edge and is strongest when we allow for cooling.

All of our evolutions reveal magnetic field lines emanating from each of the two horizons, forming dual jets which merge into one helical structure above the polar regions.

We estimate that the effective optical depth is $\tau^* \sim \mathcal{O}(1)(L_b/L_{\text{Edd}})^{9/16}(M/10^8 M_\odot)^{-1/16}$ throughout the bulk of the disk, hence the disks we consider are optically thick to absorption. The characteristic effective temperature of our disk models is $T_{\text{eff}} \sim 10^5 (L_b/L_{\text{Edd}})^{1/4} (M/10^8 M_\odot)^{-1/4}$ K. Expected frequencies of the thermal radiation are $\nu_{bb} \sim 10^{15} (L_b/L_{\text{Edd}})^{1/4} (M/10^8 M_\odot)^{-1/4} / (1+z)$ Hz (optical/near UV). Therefore, instruments such as LSST, WFIRST, and PanSTARRS will be ideally suited to study these sources. In the cavity, we find that $\tau^* < 1$, hence cyclotron lines may be directly observable as a nonthermal component of the spectrum. Typical cyclotron frequencies in the cavity then are $\nu_{cy} \sim 10^6 (M/10^8 M_\odot)^{-1/2} (L_b/L_{\text{Edd}})^{1/2} (1+z)^{-1}$ Hz, which fall in the radio spectrum. Although considerable caution must be applied to these estimates, as we do not account for microphysics and radiative transfer in our simulations, they may serve as useful guides to subse-

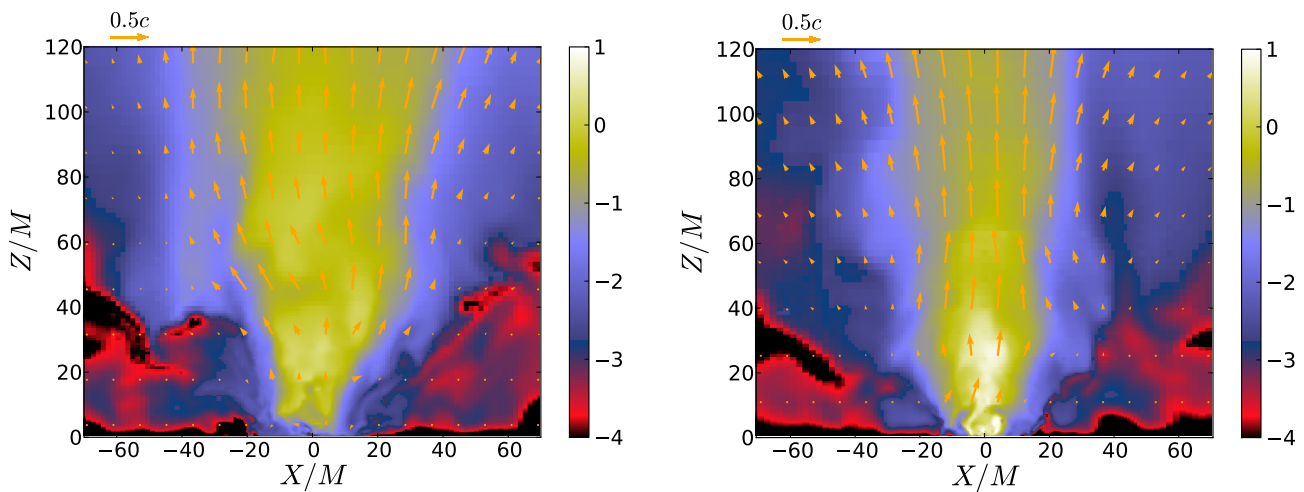


FIG. 22. Contours of $b^2/2\rho_0$, (log color scale) in a meridional slice, and fluid velocity (arrows) at $t \sim 10000M$. Left panel: $q = 1$ cooling case. Right panel: $q = 0.1$ cooling case.

quent, more detailed investigations and to astronomical instruments that may be able to observe the scenarios we are simulating.

In upcoming work we plan to evolve the models presented here through inspiral, merger, and the post-merger phases. We expect afterglow emission [37, 40] similar to [76]. The latter phase will model the process by which the disk material viscously diffuses into the cavity following merger, leading to a brightening of the disk [40, 41]. In the future we plan to include more realistic cooling and radiative transfer and use higher resolution for a more accurate modeling of these sources. It will be crucial to determine in this context the level of variability in the luminosity, and the EM spectrum of the source.

ACKNOWLEDGMENTS

It is a pleasure to thank the Illinois Relativity group REU team (Albert Kim, Lingyi Kong, Brian R. Taylor, and Francis J. Walsh) for assistance in creating Figs. 1 and 23. We thank Brian Farris for useful discussions. This paper was supported in part by NSF Grants AST-1002667, PHY-0963136 and PHY-1300903 as well as NASA Grants NNX11AE11G and NN13AH44G at the University of Illinois at Urbana-Champaign. VP gratefully acknowledges support from a Fortner Fellowship at UIUC. HPP acknowledges support by NSERC of Canada, the Canada Chairs Program, and the Canadian Institute for Advanced Research. The metric initial data was computed on the GPC supercomputer at the SciNet HPC Consortium [137]. SciNet is funded by: the Canada Foundation for Innovation under the auspices of Compute Canada; the Government of Ontario; Ontario Research Fund—Research Excellence; and the University of Toronto. This work used the Extreme Science and

Engineering Discovery Environment (XSEDE), which is supported by NSF grant number OCI-1053575. This research is part of the Blue Waters sustained-petascale computing project, which is supported by the National Science Foundation (award number OCI 07-25070) and the state of Illinois. Blue Waters is a joint effort of the University of Illinois at Urbana-Champaign and its National Center for Supercomputing Applications.

Appendix A: Numerical stability of cooling schemes in low density regions

The evolution equation for the specific thermal energy without magnetic fields, but including radiation with an effective emissivity $\Lambda = dU/d\tau$ as measured by an observer comoving with the fluid, is given by [117]

$$\frac{d\epsilon_{\text{th}}}{d\tau} = \frac{P_{\text{th}}}{\rho_0^2} \frac{d\rho_0}{d\tau} - \frac{1}{\rho_0} \Lambda, \quad (\text{A1})$$

where $\epsilon_{\text{th}} \equiv \epsilon - \epsilon_0$, and where ϵ is the total specific energy and ϵ_0 the total specific energy of the fluid element calculated with the EOS at $t = 0$, i.e., $P = K_0 \rho_0^\Gamma$, $\epsilon_0 = P/\rho_0(\Gamma - 1)$. We thus account for cooling by specifying Λ .

1. Cooling prescriptions

Two effective emissivities that have been adopted in the literature are:

$$\Lambda_1 = \frac{\rho_0 \epsilon_{\text{th}}}{\tau_c}, \quad (\text{A2})$$

where τ_c is the cooling time scale, and

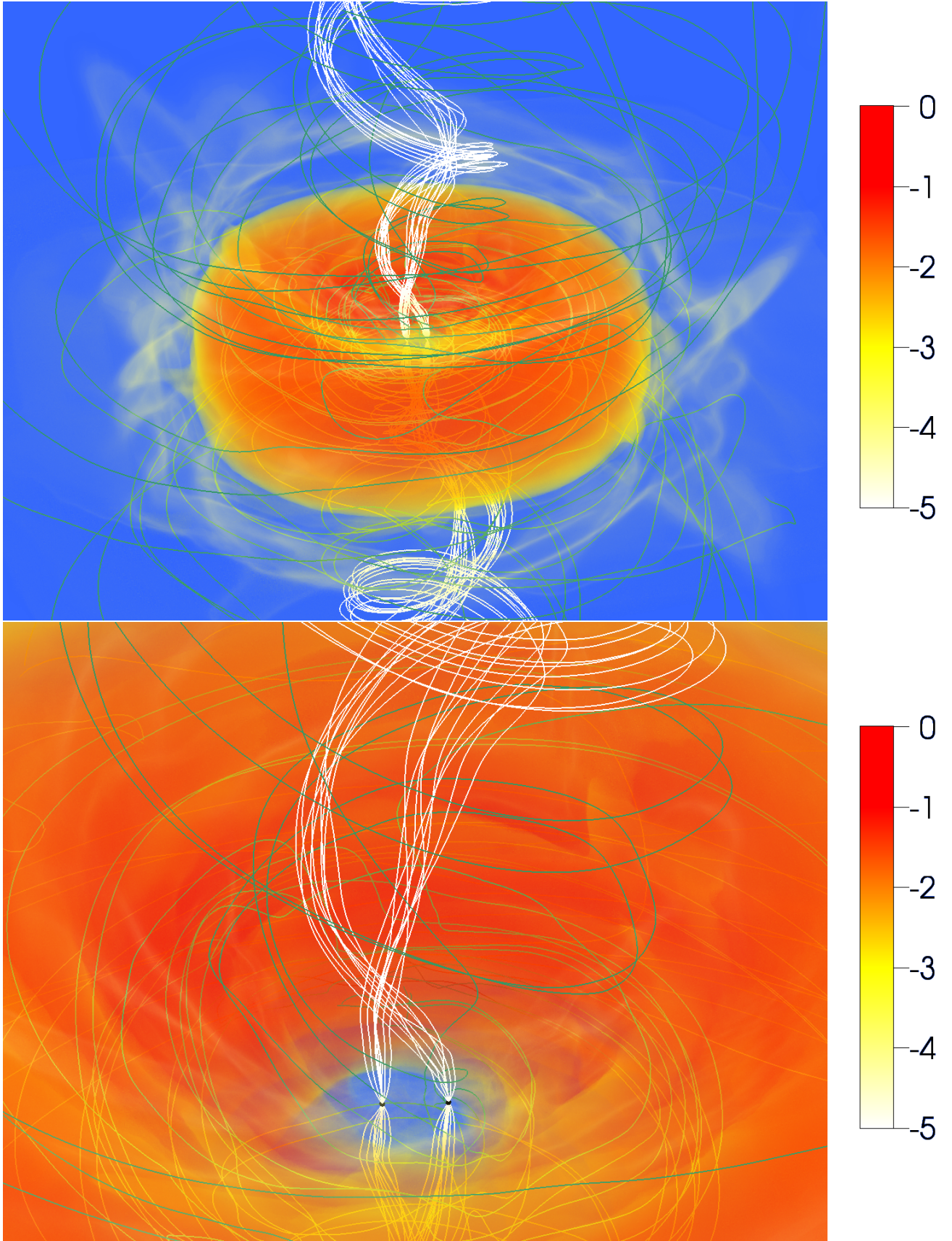


FIG. 23. Volume rendering of rest-mass density normalized to its initial maximum value (color coding) and magnetic field lines for the $q = 1$ cooling (medium resolution) case. White field lines emanate from the BH apparent horizons. Incipient jets are launched from these systems.

$$\Lambda_2 = \frac{\rho_0 \epsilon}{\tau_c} \left(\frac{\Delta S}{S_0} + \left| \frac{\Delta S}{S_0} \right| \right), \quad (\text{A3})$$

where $S \equiv K = P/\rho_0^\Gamma$ and S_0 is both the initial (unshocked) and target value. We introduced (A2) in [117], and (A3) was introduced in [72, 124]. While these two schemes achieve similar properties, i.e., drive K back to its initial value, they have fundamentally different numerical stability properties. Here we explain why this is so.

First, let us recast our cooling emissivity Λ_1 in a form that is similar to Λ_2 to show that our cooling prescription also drives K to K_0 . The pressure is given by

$$P = \rho_0 \epsilon (\Gamma - 1) \quad (\text{A4})$$

and similarly for the initial pressure

$$P_0 = \rho_0 \epsilon_0 (\Gamma - 1). \quad (\text{A5})$$

The difference between the two is

$$\Delta P = \rho_0 (\epsilon - \epsilon_0) (\Gamma - 1) = \rho_0 \epsilon_{\text{th}} (\Gamma - 1) = P_0 \frac{\epsilon_{\text{th}}}{\epsilon_0}. \quad (\text{A6})$$

But,

$$\frac{\Delta P}{P_0} = \frac{(K - K_0) \rho_0^\Gamma}{K_0 \rho_0^\Gamma} = \frac{\Delta K}{K_0} = \frac{\Delta S}{S_0}. \quad (\text{A7})$$

Combining Eqs. (A6), (A7), and (A2) yields

$$\Lambda_1 = \frac{\rho_0 \epsilon_0}{\tau_c} \frac{\Delta S}{S_0}. \quad (\text{A8})$$

The emissivity Λ_2 for $\Delta S > 0$, i.e., the only case when the emissivity is not 0, becomes

$$\Lambda_2 = \frac{2\rho_0 \epsilon}{\tau_c} \frac{\Delta S}{S_0}. \quad (\text{A9})$$

Thus, the two prescriptions Eqs. (A8) and (A9) are similar and both drive the gas to constant initial entropy S_0 . But the two prescriptions are not the same. Another way to see this is to write Λ_2 in a form that resembles Λ_1 . Using Eqs. (A6), (A7), we can write (A9) as

$$\Lambda_2 = \frac{2\rho_0 \epsilon_{\text{th}}}{\tau_c} \frac{\epsilon}{\epsilon_0}. \quad (\text{A10})$$

As we will see below, it is the factor ϵ/ϵ_0 by which Λ_2 differs from Λ_1 that leads to the completely different numerical stability properties of these two cooling schemes.

2. Numerical properties of cooling prescriptions

Insert our cooling prescription in Eq. (A1) and drop the first term on the right-hand-side (RHS) of Eq. (A1), i.e., assume that no adiabatic compression or expansion takes place. Then we obtain

$$\frac{d\epsilon_{\text{th}}}{d\tau} = -\frac{\epsilon_{\text{th}}}{\tau_c}, \quad (\text{A11})$$

i.e., exponential cooling of the excess thermal energy with cooling time scale τ_c . For an explicit numerical scheme to be Courant stable we must set the maximum timestep $\Delta t \lesssim \tau_c$. To see this we can use a simple Euler explicit integration scheme to write Eq. (A11) in finite difference form as

$$\frac{\epsilon_{\text{th}}^{n+1} - \epsilon_{\text{th}}^n}{\Delta\tau} = -\frac{\epsilon_{\text{th}}^n}{\tau_c}. \quad (\text{A12})$$

Then the amplification factor is given by

$$f \equiv \frac{\epsilon_{\text{th}}^{n+1}}{\epsilon_{\text{th}}^n} = 1 - \frac{\Delta\tau}{\tau_c}. \quad (\text{A13})$$

For numerical stability the magnitude of the amplification factor must be less than 1

$$|f| < 1 \Rightarrow \left| 1 - \frac{\Delta\tau}{\tau_c} \right| < 1 \Rightarrow \Delta\tau < 2\tau_c. \quad (\text{A14})$$

By contrast, inserting Λ_2 [Eq. (A10)] in Eq. (A1) and dropping the first term on the RHS of Eq. (A1) yields

$$\frac{d\epsilon_{\text{th}}}{d\tau} = -2 \frac{\epsilon_{\text{th}}}{\tau_c} \frac{\epsilon}{\epsilon_0}, \quad (\text{A15})$$

hence the effective cooling time scale is now

$$\tau_{\text{eff}} = \frac{1}{2} \frac{\epsilon_0}{\epsilon} \tau_c. \quad (\text{A16})$$

We now require $\Delta t < \tau_{\text{eff}}$ for numerical stability. However, low density regions can become strongly shock heated, in which case $\epsilon_0 \ll \epsilon$, implying $\tau_{\text{eff}} \ll \tau_c$. As a result, a violation of the Courant stability condition can quickly occur that will terminate the computations, if $\Delta t < \tau_c$ is used as the stability condition. This is a disadvantage of the Λ_2 prescription, as it means that one must impose a density cutoff for the simulations to be stable and retain relatively large timesteps. This is something we do not need to require with our cooling emissivity Λ_1 , as the fixed cooling time scale τ_c is, at the same time, the effective cooling time scale. The difference is important as we want to probe low density regimes in the disk without artificial cutoffs.

- [1] M. Begelman, R. Blandford, and M. Rees, *Nature* **287**, 307 (1980)
- [2] P. Ivanov, J. Papaloizou, and A. Polnarev(1998), arXiv:astro-ph/9812198 [astro-ph]
- [3] Z. Haiman, B. Kocsis, and K. Menou, *Astrophys.J.* **700**, 1952 (2009), arXiv:0904.1383 [astro-ph.CO]
- [4] R. R. Rafikov(2012), arXiv:1205.5017 [astro-ph.GA]
- [5] P. J. Armitage and P. Natarajan, *Astrophys.J.* **567**, L9 (2002), arXiv:astro-ph/0201318 [astro-ph]
- [6] P. J. Armitage and P. Natarajan, *Astrophys.J.* **634**, 921 (2005), arXiv:astro-ph/0508493 [astro-ph]
- [7] M. Milosavljevic and D. Merritt, *Astrophys.J.* **563**, 34 (2001), arXiv:astro-ph/0103350 [astro-ph]
- [8] M. Milosavljevic and D. Merritt, *AIP Conf.Proc.* **686**, 201 (2003), arXiv:astro-ph/0212270 [astro-ph]
- [9] D. Merritt and M. Milosavljevic, *Living Rev.Rel.* **8**, 8 (2005), arXiv:astro-ph/0410364 [astro-ph]
- [10] F. Khan and K. Holley-Bockelmann(2013), arXiv:1302.1871 [astro-ph.GA]
- [11] M. Dotti, A. Sesana, and R. Decarli, *Adv.Astron.* **2012**, 940568 (2012), arXiv:1111.0664 [astro-ph.CO]
- [12] B. F. Schutz, *Nature* **323**, 310 (1986)
- [13] D. E. Holz and S. A. Hughes, *Astrophys.J.* **629**, 15 (2005), arXiv:astro-ph/0504616 [astro-ph]
- [14] S. Nissanke, D. E. Holz, N. Dalal, S. A. Hughes, J. L. Sievers, et al.(2013), arXiv:1307.2638 [astro-ph.CO]
- [15] P. Amaro-Seoane, S. Aoudia, S. Babak, P. Binétruy, E. Berti, et al.(2012), arXiv:1201.3621 [astro-ph.CO]
- [16] G. Hobbs, A. Archibald, Z. Arzoumanian, D. Backer, M. Bailes, et al., *Class.Quant.Grav.* **27**, 084013 (2010), arXiv:0911.5206 [astro-ph.SR]
- [17] T. Tanaka, Z. Haiman, and K. Menou(2011), arXiv:1107.2937 [astro-ph.CO]
- [18] A. Sesana(2012), arXiv:1211.5375 [astro-ph.CO]
- [19] P. A. Abell et al. (LSST Science Collaborations, LSST Project)(2009), arXiv:0912.0201 [astro-ph.IM]
- [20] J. Green, P. Schechter, C. Baltay, R. Bean, D. Bennett, et al.(2012), arXiv:1208.4012 [astro-ph.IM]
- [21] N. Kaiser, H. Aussel, H. Boesgaard, K. Chambers, J. N. Heasley, et al., *Proc.SPIE Int.Soc.Opt.Eng.* **4836**, 154 (2002)
- [22] C. Rodriguez, G. B. Taylor, R. Zavala, A. Peck, L. Pollack, et al., *Astrophys.J.* **646**, 49 (2006), arXiv:astro-ph/0604042 [astro-ph]
- [23] A. Sillanpaa, S. Haarala, M. J. Valtonen, B. Sundelius, and G. G. Byrd, *Astrophys. J.* **325**, 628 (Feb. 1988)
- [24] H. J. Lehto and M. J. Valtonen, *Astrophys. J.* **460**, 207 (Mar. 1996)
- [25] M. Valtonen and S. Ciprini(2011), arXiv:1112.1162 [astro-ph.HE]
- [26] T. L. Tanaka(2013), arXiv:1303.6279 [astro-ph.CO]
- [27] T. A. Boroson and T. R. Lauer(2009), arXiv:0901.3779 [astro-ph.GA]
- [28] R. Chornock, J. S. Bloom, S. B. Cenko, J. M. Silverman, A. V. Filippenko, M. D. Hicks, K. J. Lawrence, P. Chang, J. M. Comerford, M. R. George, M. Modjaz, J. S. Oishi, E. Quataert, and L. E. Strubbe, *The Astronomer's Telegram* **1955**, 1 (Mar. 2009)
- [29] R. Decarli, M. Dotti, M. Fumagalli, P. Tsalmantza, C. Montuori, et al.(2013), arXiv:1305.4941 [astro-ph.CO]
- [30] M. Eracleous, T. A. Boroson, J. P. Halpern, and J. Liu(2011), arXiv:1106.2952 [astro-ph.CO]
- [31] J. Roland, S. Britzen, A. Caproni, C. Fromm, C. Glück, et al.(2013), arXiv:1307.3700 [astro-ph.HE]
- [32] S. Komossa, *Adv.Astron.* **2012**, 364973 (2012), arXiv:1202.1977 [astro-ph.CO]
- [33] G. E. Romero, L. Chajet, Z. Abraham, and J. H. Fan, *Astron. and Astrophys.* **360**, 57 (Aug. 2000)
- [34] N. Roos, J. S. Kaastra, and C. A. Hummel, *Astrophys. J.* **409**, 130 (May 1993)
- [35] H. Sudou, S. Iguchi, Y. Murata, and Y. Taniguchi, *Science* **300**, 1263 (2003), arXiv:astro-ph/0306103 [astro-ph]
- [36] B. McKernan, K. Ford, B. Kocsis, and Z. Haiman(2013), arXiv:1303.7206 [astro-ph.HE]
- [37] M. Milosavljevic and E. Phinney, *Astrophys.J.* **622**, L93 (2005), arXiv:astro-ph/0410343 [astro-ph]
- [38] B. Kocsis, Z. Haiman, and K. Menou, *Astrophys.J.* **684**, 870 (2008), arXiv:0712.1144 [astro-ph]
- [39] Z. Haiman, B. Kocsis, K. Menou, Z. Lippai, and Z. Frei, *Class.Quant.Grav.* **26**, 094032 (2009), arXiv:0811.1920 [astro-ph]
- [40] T. Tanaka and K. Menou, *Astrophys.J.* **714**, 404 (2010), arXiv:0912.2054 [astro-ph.CO]
- [41] S. L. Shapiro, *Phys.Rev.* **D81**, 024019 (2010), arXiv:0912.2345 [astro-ph.HE]
- [42] Y. T. Liu and S. L. Shapiro, *Phys.Rev.* **D82**, 123011 (2010), arXiv:1011.0002 [astro-ph.HE]
- [43] S. L. Shapiro, *Phys.Rev.* **D87**, 103009 (2013), arXiv:1304.6090 [astro-ph.HE]
- [44] H. Bondi and F. Hoyle, *Mon. Not. R. Astron. Soc.* **104**, 273 (1944)
- [45] H. Bondi, *Mon. Not. R. Astron. Soc.* **112**, 195 (1952)
- [46] L. I. Petrich, S. L. Shapiro, R. F. Stark, and S. A. Teukolsky, *Astrophys. J.* **336**, 313 (Jan. 1989)
- [47] B. D. Farris, Y. T. Liu, and S. L. Shapiro, *Phys.Rev.* **D81**, 084008 (2010), arXiv:0912.2096 [astro-ph.HE]
- [48] O. Zanotti, C. Roedig, L. Rezzolla, and L. Del Zanna, *Mon.Not.Roy.Astron.Soc.* **417**, 2899 (2011), arXiv:1105.5615 [astro-ph.HE]
- [49] B. Giacomazzo, J. G. Baker, M. C. Miller, C. S. Reynolds, and J. R. van Meter, *Astrophys.J.* **752**, L15 (2012), arXiv:1203.6108 [astro-ph.HE]
- [50] M. A. Abramowicz and P. C. Fragile, *Living Reviews in Relativity* **16** (2013), doi:"bibinfo doi 10.12942/lrr-2013-1", <http://www.livingreviews.org/lrr-2013-1>
- [51] N. I. Shakura and R. A. Sunyaev, *Astron. and Astrophys.* **24**, 337 (1973)
- [52] I. D. Novikov and K. S. Thorne, in *Black Holes (Les Astres Occlus)* (1973) pp. 343–450
- [53] M. A. Abramowicz, B. Czerny, J. P. Lasota, and E. Szuszkiewicz, *Astrophys. J.* **332**, 646 (Sep. 1988)
- [54] S. Ichimaru, *Astrophys. J.* **214**, 840 (Jun. 1977)
- [55] R. D. Blandford and M. C. Begelman, *Mon.Not.Roy.Astron.Soc.* **303**, L1 (1999), arXiv:astro-ph/9809083 [astro-ph]
- [56] I. Igmenshchev, M. Abramowicz, and I. Novikov(1997), arXiv:astro-ph/9709156 [astro-ph]
- [57] A. A. Esin, J. E. McClintock, and R. Narayan, *Astrophys.J.* **489**, 865 (1997), arXiv:astro-ph/9705237 [astro-ph]

- [58] R. Narayan(1996), arXiv:astro-ph/9611113 [astro-ph]
- [59] P. Artymowicz and S. H. Lubow, *Astrophys.J.* **421**, 651 (1994)
- [60] B. Kocsis, Z. Haiman, and A. Loeb, *Mon.Not.Roy.Astron.Soc.* **427**, 2680 (2012), arXiv:1205.5268 [astro-ph.HE]
- [61] B. Kocsis, Z. Haiman, and A. Loeb, *Mon.Not.Roy.Astron.Soc.* **427**, 2660 (2012), arXiv:1205.4714 [astro-ph.EP]
- [62] P. Artymowicz and S. H. Lubow, *Astrophys.J.* **467**, L77 (1996)
- [63] A. I. MacFadyen and M. Milosavljevic, *Astrophys.J.* **672**, 83 (2008), arXiv:astro-ph/0607467 [astro-ph]
- [64] D. J. D’Orazio, Z. Haiman, and A. MacFadyen(2012), arXiv:1210.0536 [astro-ph.GA]
- [65] B. D. Farris, P. Duffell, A. I. MacFadyen, and Z. Haiman(2013), arXiv:1310.0492 [astro-ph.HE]
- [66] M. Dotti, M. Colpi, F. Haardt, and L. Mayer, *Mon.Not.Roy.Astron.Soc.* **379**, 956 (2007), arXiv:astro-ph/0612505 [astro-ph]
- [67] J. Cuadra, P. Armitage, R. Alexander, and M. Begelman(2008), arXiv:0809.0311 [astro-ph]
- [68] C. Roedig, M. Dotti, A. Sesana, J. Cuadra, and M. Colpi(2011), arXiv:1104.3868 [astro-ph.CO]
- [69] C. Roedig, A. Sesana, M. Dotti, J. Cuadra, P. Amaro-Seoane, et al.(2012), arXiv:1202.6063 [astro-ph.CO]
- [70] K. Hayasaki, H. Saito, and S. Mineshige(2012), arXiv:1211.5137 [astro-ph.GA]
- [71] J.-M. Shi, J. H. Krolik, S. H. Lubow, and J. F. Hawley, *Astrophys.J.* **749**, 118 (2012), arXiv:1110.4866 [astro-ph.HE]
- [72] S. C. Noble, B. C. Mundim, H. Nakano, J. H. Krolik, M. Campanelli, et al., *Astrophys.J.* **755**, 51 (2012), arXiv:1204.1073 [astro-ph.HE]
- [73] T. Bode, R. Haas, T. Bogdanovic, P. Laguna, and D. Shoemaker, *Astrophys.J.* **715**, 1117 (2010), arXiv:0912.0087 [gr-qc]
- [74] T. Bogdanovic, T. Bode, R. Haas, P. Laguna, and D. Shoemaker, *Class.Quant.Grav.* **28**, 094020 (2011), arXiv:1010.2496 [astro-ph.CO]
- [75] T. Bode, T. Bogdanovic, R. Haas, J. Healy, P. Laguna, et al., *Astrophys.J.* **744**, 45 (2012), arXiv:1101.4684 [gr-qc]
- [76] B. D. Farris, R. Gold, V. Paschalidis, Z. B. Etienne, and S. L. Shapiro, *Phys.Rev.Lett.* **109**, 221102 (2012), arXiv:1207.3354 [astro-ph.HE]
- [77] P. Mosta, C. Palenzuela, L. Rezzolla, L. Lehner, S. Yoshida, et al., *Phys.Rev.* **D81**, 064017 (2010), arXiv:0912.2330 [gr-qc]
- [78] D. Neilsen, L. Lehner, C. Palenzuela, E. W. Hirschmann, S. L. Liebling, et al., *Proc.Nat.Acad.Sci.* **108**, 12641 (2011), arXiv:1012.5661 [astro-ph.HE]
- [79] C. Palenzuela, T. Garrett, L. Lehner, and S. L. Liebling, *Phys.Rev.* **D82**, 044045 (2010), arXiv:1007.1198 [gr-qc]
- [80] C. Palenzuela, L. Lehner, and S. L. Liebling, *Science* **329**, 927 (2010), arXiv:1005.1067 [astro-ph.HE]
- [81] L. R. Corrales, Z. Haiman, and A. MacFadyen(2009), arXiv:0910.0014 [astro-ph.HE]
- [82] E. M. Rossi, G. Lodato, P. Armitage, J. Pringle, and A. King(2009), arXiv:0910.0002 [astro-ph.HE]
- [83] M. Anderson, L. Lehner, M. Megevand, and D. Neilsen, *Phys.Rev.* **D81**, 044004 (2010), arXiv:0910.4969 [astro-ph.HE]
- [84] M. Megevand, M. Anderson, J. Frank, E. W. Hirschmann, L. Lehner, et al., *Phys.Rev.* **D80**, 024012 (2009), arXiv:0905.3390 [astro-ph.HE]
- [85] M. Ponce, J. A. Faber, and J. Lombardi, James C., *Astrophys.J.* **745**, 71 (2012), arXiv:1107.1711 [astro-ph.CO]
- [86] L. A. Gergely and P. L. Biermann, *Astrophys.J.* **697**, 1621 (2009), arXiv:0704.1968 [astro-ph]
- [87] A. Sesana, M. Volonteri, and F. Haardt, *Mon.Not.Roy.Astron.Soc.* **377**, 1711 (2007), arXiv:astro-ph/0701556 [astro-ph]
- [88] A. Sesana, C. Roedig, M. Reynolds, and M. Dotti(2011), arXiv:1107.2927 [astro-ph.CO]
- [89] S. A. Balbus and J. F. Hawley, *Astrophys.J.* **376**, 214 (1991)
- [90] S. A. Balbus and J. F. Hawley, *Rev.Mod.Phys.* **70**, 1 (1998)
- [91] H. P. Pfeiffer and J. York, James W., *Phys.Rev.* **D67**, 044022 (2003), arXiv:gr-qc/0207095 [gr-qc]
- [92] G. B. Cook and H. P. Pfeiffer, *Phys.Rev.* **D70**, 104016 (2004), arXiv:gr-qc/0407078 [gr-qc]
- [93] M. Caudill, G. B. Cook, J. D. Grigsby, and H. P. Pfeiffer, *Phys.Rev.* **D74**, 064011 (2006), arXiv:gr-qc/0605053 [gr-qc]
- [94] T. W. Baumgarte and S. L. Shapiro, *Solving Einstein’s Equations on the Computer* (Cambridge University Press, 2010)
- [95] B. D. Farris, Y. T. Liu, and S. L. Shapiro, *Phys.Rev.* **D84**, 024024 (2011), arXiv:1105.2821 [astro-ph.HE]
- [96] T. M. Heckman, G. Kauffmann, J. Brinchmann, S. Charlot, C. Tremonti, et al., *Astrophys.J.* **613**, 109 (2004), arXiv:astro-ph/0406218 [astro-ph]
- [97] Y. Shen and B. C. Kelly, *Astrophys.J.* **746**, 169 (2012), arXiv:1107.4372 [astro-ph.CO]
- [98] B. C. Kelly and Y. Shen, *Astrophys.J.* **764**, 45 (2013), arXiv:1209.0477 [astro-ph.CO]
- [99] J. A. Kollmeier, C. A. Onken, C. S. Kochanek, A. Gould, D. H. Weinberg, et al., *Astrophys.J.* **648**, 128 (2006), arXiv:astro-ph/0508657 [astro-ph]
- [100] E. Lusso, A. Comastri, B. Simmons, M. Mignoli, G. Zamorani, et al.(2012), arXiv:1206.2642 [astro-ph.CO]
- [101] A. Schulze and L. Wisotzki(2010), arXiv:1004.2671 [astro-ph.CO]
- [102] D. J. Mortlock, S. J. Warren, B. P. Venemans, M. Patel, P. C. Hewett, et al., *Nature* **474**, 616 (2011), arXiv:1106.6088 [astro-ph.CO]
- [103] J. Goodman, *Mon.Not.Roy.Astron.Soc.* **339**, 937 (2003), arXiv:astro-ph/0201001 [astro-ph]
- [104] C. Roedig and A. Sesana, *J.Phys.Conf.Ser.* **363**, 012035 (2012), arXiv:1111.3742 [astro-ph.CO]
- [105] H. P. Pfeiffer, L. E. Kidder, M. A. Scheel, and S. A. Teukolsky, *Comput.Phys.Commun.* **152**, 253 (2003), arXiv:gr-qc/0202096 [gr-qc]
- [106] <http://www.black-holes.org/SpEC.html>
- [107] A. H. Mroue, M. A. Scheel, B. Szilagyi, H. P. Pfeiffer, M. Boyle, et al.(2013), arXiv:1304.6077 [gr-qc]
- [108] S. K. Chakrabarti, *Astrophys. J.* **288**, 1 (Jan. 1985)
- [109] J.-P. De Villiers, J. F. Hawley, and J. H. Krolik(2003), arXiv:astro-ph/0307260 [astro-ph]
- [110] Z. B. Etienne, Y. T. Liu, V. Paschalidis, and S. L. Shapiro, *Phys.Rev.* **D85**, 064029 (2012), arXiv:1112.0568 [astro-ph.HE]
- [111] M. D. Duez, Y. T. Liu, S. L. Shapiro, and B. C. Stephens, *Phys.Rev.* **D72**, 024028 (2005), arXiv:astro-

- ph/0503420 [astro-ph]
- [112] Z. B. Etienne, Y. T. Liu, and S. L. Shapiro, *Phys.Rev.* **D82**, 084031 (2010), arXiv:1007.2848 [astro-ph.HE]
- [113] Z. B. Etienne, V. Paschalidis, Y. T. Liu, and S. L. Shapiro, *Phys.Rev.* **D85**, 024013 (2012), arXiv:1110.4633 [astro-ph.HE]
- [114] T. Goodale, G. Allen, G. Lanfermann, J. Massó, T. Radke, E. Seidel, and J. Shalf, in *5th Int. Conference, Lecture Notes in Comp. Science* (Springer, Berlin, 2003) <http://edoc.mpg.de/3341>
- [115] “Cactus Computational Toolkit,” <http://www.cactuscode.org/>
- [116] “Mesh refinement with Carpet,” <http://www.carpetcode.org/>
- [117] V. Paschalidis, Y. T. Liu, Z. Etienne, and S. L. Shapiro, *Phys.Rev.* **D84**, 104032 (2011), arXiv:1109.5177 [astro-ph.HE]
- [118] Z. B. Etienne, V. Paschalidis, and S. L. Shapiro, *Phys.Rev.* **D86**, 084026 (2012), arXiv:1209.1632 [astro-ph.HE]
- [119] V. Paschalidis, Z. B. Etienne, and S. L. Shapiro, *Phys.Rev.* **D86**, 064032 (2012), arXiv:1208.5487 [astro-ph.HE]
- [120] Z. B. Etienne, Y. T. Liu, V. Paschalidis, and S. L. Shapiro(2013), arXiv:1303.0837 [astro-ph.HE]
- [121] V. Paschalidis, Z. B. Etienne, and S. L. Shapiro(2013), arXiv:1304.1805 [astro-ph.HE]
- [122] L. Rezzolla, B. Giacomazzo, L. Baiotti, J. Granot, C. Kouveliotou, et al., *Astrophys.J.* **732**, L6 (2011), arXiv:1101.4298 [astro-ph.HE]
- [123] M. D. Duez, P. Marronetti, S. L. Shapiro, and T. W. Baumgarte, *Phys.Rev.* **D67**, 024004 (2003), arXiv:gr-qc/0209102 [gr-qc]
- [124] R. Shafee, J. C. McKinney, R. Narayan, A. Tchekhovskoy, C. F. Gammie, et al.(2008), arXiv:0808.2860 [astro-ph]
- [125] Z. B. Etienne, Y. T. Liu, S. L. Shapiro, and T. W. Baumgarte, *Phys.Rev.* **D79**, 044024 (2009), arXiv:0812.2245 [astro-ph]
- [126] R. F. Penna, J. C. McKinney, R. Narayan, A. Tchekhovskoy, R. Shafee, et al., *Mon.Not.Roy.Astron.Soc.* **408**, 752 (2010), arXiv:1003.0966 [astro-ph.HE]
- [127] S. L. Shapiro and S. A. Teukolsky, New York, Wiley-Interscience, 1983, 663 p. (1983)
- [128] M. Shibata, Y. T. Liu, S. L. Shapiro, and B. C. Stephens, *Phys.Rev.* **D74**, 104026 (2006), arXiv:astro-ph/0610840 [astro-ph]
- [129] T. Sano, S.-i. Inutsuka, N. J. Turner, and J. M. Stone, *Astrophys.J.* **605**, 321 (2004), arXiv:astro-ph/0312480 [astro-ph]
- [130] H. Shiokawa, J. C. Dolence, C. F. Gammie, and S. C. Noble, *Astrophys. J.* **744**, 187 (Jan. 2012)
- [131] Condition (III) is satisfied everywhere shortly after our evolutions begin because magnetic winding converts poloidal magnetic field into toroidal, thereby decreasing λ_{MRI} . Our high-resolution grids satisfy condition (II) in the innermost parts of the disk even after the evolution begins.
- [132] T. L. Tanaka and Z. Haiman(2013), arXiv:1309.2302 [astro-ph.CO]
- [133] D. N. C. Lin and J. C. B. Papaloizou, in *Protostars and Planets III*, edited by E. H. Levy and J. I. Lunine (1993) pp. 749–835
- [134] D. Lynden-Bell and M. J. Rees, *Mon. Not. R. Astron. Soc.* **152**, 461 (1971)
- [135] P. Moesta, D. Alic, L. Rezzolla, O. Zanotti, and C. Palenzuela, *Astrophys.J.* **749**, L32 (2012), arXiv:1109.1177 [gr-qc]
- [136] M. Coleman Miller and J. H. Krolik, *Astrophys.J.* **774**, 43 (2013), arXiv:1307.6569 [astro-ph.HE]
- [137] C. Loken, D. Gruner, L. Groer, R. Peltier, N. Bunn, M. Craig, T. Henriques, J. Dempsey, C.-H. Yu, J. Chen, L. J. Dursi, J. Chong, S. Northrup, J. Pinto, N. Knecht, and R. V. Zon, *J. Phys.: Conf. Ser.* **256**, 012026 (2010)